

YunMa: Enabling Spectral Retrievals of Exoplanetary Clouds

SUSHUANG MA ¹, YUICHI ITO ^{2,1}, AHMED FARIS AL-REFAIE ¹, QUENTIN CHANGEAT ^{3,1}, BILLY EDWARDS ^{4,5,1} AND GIOVANNA TINETTI ¹

¹*Department of Physics and Astronomy, University College London
Gower Street, WC1E 6BT London, United Kingdom*

²*National Astronomical Observatory of Japan
2 Chome-21-1 Osawa, Mitaka, Tokyo, 181-8588, Japan*

³*European Space Agency (ESA)*

ESA Office, Space Telescope Science Institute (STScI), 3700 San Martin Drive, Baltimore MD 21218, United States of America

⁴*SRON, Netherlands Institute for Space Research, Niels Bohrweg 4, NL-2333 CA, Leiden, The Netherlands*

⁵*AIM, CEA, CNRS, Université Paris-Saclay, Université de Paris, F-91191 Gif-sur-Yvette, France*

ABSTRACT

In this paper, we present *YunMa*, a model which enables the study of cloud microphysics and radiative properties in exoplanetary atmospheres. *YunMa* simulates the vertical distribution and sizes of cloud particles and their corresponding scattering signature in transit spectra. We validated *YunMa* against results from the literature.

When coupled to the *TauREx 3* platform, an open Bayesian framework for spectral retrievals, *YunMa* enables the retrieval of the cloud properties and parameters from transit spectra of exoplanets. The sedimentation efficiency (f_{sed}), which controls the cloud microphysics, is set as a free parameter in retrievals. We assess the retrieval performances of *YunMa* through 28 instances of a cloudy super-Earth's atmosphere. This work also highlights the need for cloud radiative transfer and microphysics modelling to retrieve next-generation data of exoplanets.

Keywords: Exoplanets(498) — Exoplanet atmospheres(487) — Transmission spectroscopy(2133) — Atmospheric clouds(2180)

1. INTRODUCTION

Thousands of exoplanets have been detected since the late 20th century. During the past decade, transit spectroscopy has become one of the most powerful techniques for studying exoplanets' atmospheres in-depth (e.g., reviews by Tinetti et al. 2013; Burrows 2014; Madhusudhan 2019). Data recorded from space-borne instruments (e.g., Hubble, Spitzer and James Webb Space Telescopes) or from the ground have revealed important information about exoplanet atmospheric chemistry and dynamics (e.g., Sing et al. 2016; Tsiaras et al. 2018; Welbanks et al. 2019; Changeat et al. 2022; Edwards et al. 2022; JWST Transiting Exoplanet Community Early Release Science Team 2022; Venot et al. 2020; Roudier et al. 2021) and may provide insight into planetary in-

terior composition and formation (Madhusudhan et al. 2020; Yu et al. 2021; Tsai et al. 2021; Charnay et al. 2022).

A number of spectral retrieval models have been developed by different teams to interpret the atmospheric data and quantify their information content; these include e.g., Madhusudhan & Seager (2009), Lee et al. (2012), TauREx 3 (Al-Refaie et al. 2021), NEMESIS (Irwin et al. 2008), CHIMERA (Line et al. 2013), AR-CiS (Min et al. 2020; Ormel & Min 2019), PICASO (Robbins-Blanch et al. 2022; Batalha et al. 2019), BART (Harrington et al. 2022), petitRADTRANS (Mollière, P. et al. 2020), HELIOS (Kitzmann et al. 2020), POSEIDON (MacDonald & Madhusudhan 2017), HyDRA (Gandhi & Madhusudhan 2018), SCARLET (Benneke 2015), PLATON II (Zhang et al. 2020), and Pyrat-Bay (Cubillos & Blečić 2021). Up to date, most of the retrieval studies of exoplanetary atmospheres are highly parameterised. This approach has been very sensible

given the relatively poor information content of current atmospheric data. However, a number of papers in the literature (e.g., [Caldas et al. 2019](#); [Changeat et al. 2021a](#); [Changeat et al. 2022](#)) have cautioned against this approach when applied to data recorded with next-generation facilities.

Clouds are omnipresent in planetary, exoplanetary and brown dwarf atmospheres (see e.g., review by [Helling 2022](#)) and have often been detected in exoplanet atmospheric data ([Kreidberg et al. 2014](#); [Sing et al. 2016](#); [Stevenson 2016](#); [Tsiaras et al. 2018](#)). Their presence imposes additional complexity and uncertainties in the interpretation of exoplanet atmospheric spectra (e.g., [Changeat et al. 2021b](#); [Tsiaras et al. 2019](#); [Mai & Line 2019](#)).

Models simulating the formation and radiative properties of clouds and hazes have been published in the literature, e.g., [Exo-REM](#) ([Baudino et al. 2015](#); [Charnay et al. 2018](#)), [Gao et al. \(2020\)](#), [Windsor et al. \(2022\)](#) and [Kawashima & Ikoma \(2018\)](#).

Due to the – currently limited – observational constraints and computational resources available to simulate the complexity of clouds, retrieval studies of cloudy atmospheres are still in their infancy (see e.g., [Fortney et al. 2021](#)). For instance, many studies have adopted wavelength-independent opaque clouds, where all the radiation beneath the cloud top is blocked from reaching the telescope, and retrieve the vertical location of clouds ([Boucher et al. 2021](#); [Brogi & Line 2019](#)). [Wakeford et al. \(2018\)](#) used a grey, uniform cloud in the ATMO Retrieval Code (ARC) ([Goyal et al. 2017](#); [Drummond, B. et al. 2016](#); [Tremblin et al. 2015](#)). Other models constrain from radiative transfer the uniform cloud particle sizes without being estimated through cloud microphysics models. For instance, [Benneke et al. \(2019 a\)](#) have initially estimated the particle sizes in the atmosphere of GJ 3470 b using Mie-scattering theory. Extended from this highly parametric approach, cloud scattering parameters and inhomogeneous coverage were also retrieved: NEMESIS was used by [Barstow \(2020\)](#) and [Wang et al. \(2022\)](#) to retrieve the cloud’s opacity, scattering index, top and base pressures, particle sizes and shape factor. [Pinhas et al. \(2019\)](#) run POSEIDON to constrain the cloud’s top pressure and coverage fraction. [Wang et al. \(2022\)](#) adopted PICASO to extract the cloud’s base pressure, optical thickness, single scattering albedo, scattering asymmetry and coverage. [Lueber et al. \(2022\)](#) extended the use of Helios-r2 to retrieve non-grey clouds, with extinction efficiencies estimated from Mie theory calculations. The model Aurora ([Welbanks & Madhusudhan 2021](#)) presents inhomogeneities

in cloud and haze distributions by separating the atmosphere horizontally into four distinct areas.

The data provided by the next-generation telescopes will be greatly superior in quality and quantity, allowing us to obtain more stringent constraints to our understanding of clouds in exoplanetary atmospheres. Transit spectra of exoplanets recorded from space by the James Webb Space Telescope (JWST, 0.6–28.3 μm , [Bean et al. 2018](#); [Greene et al. 2016](#); [Gardner et al. 2006](#)), Ariel (0.5–7.8 μm , [Tinetti et al. 2018](#); [Tinetti et al. 2021](#)) and Tinkle (0.5–4.5 μm , [Edwards et al. 2019](#)) at relatively high spectral resolution and/or broad wavelength coverage will open the possibility of integrating self-consistent, cloud microphysics approaches into atmospheric retrieval codes. A good example of such models is ARCiS (ARtful modelling Code for exoplanet Science, [Min et al. 2020](#); [Ormel & Min 2019](#)), which simulates cloud formation from diffusion processes and parametric coagulation. ARCiS also generates cloudy transit spectra from Mie theory ([Fleck & Canfield 1984](#)) and Distribution of Hollow Spheres (DHS, [Min, M. et al. 2005](#); [Mollière, P. et al. 2019](#)), and can be used to retrieve the cloud diffusivity and nuclei injection from transit spectra.

In this work, we present a new optimised model to study cloud microphysical processes directly integrated into a spectral retrieval framework. We consider clouds as a thermochemical product, i.e. the aggregation of condensates in the atmosphere, while hazes form photochemically ([Kawashima & Ikoma 2018](#)). The cloud distribution depends on the atmospheric conditions. Being generated thermochemically, clouds form and diffuse depending on the atmospheric thermal structure and, in return, contribute to it. They also depend on the mixing profiles of the condensable gases in the atmosphere. Clouds act as absorbers and/or scatterers and therefore may dampen the atomic and molecular spectroscopic features and change the continuum.

Based on studies of the Earth and Solar System’s planetary atmospheres, [Lewis \(1969\)](#) published a 1-D cloud model optimised to describe tropospheric clouds in giant planets. This model assumes that the fall speeds of all condensates are equivalent to the updraft velocities, and only vapour is transported upward. [Lumine et al. \(1989\)](#) included a correlation between cloud particle sizes, downward sedimentation and upward turbulent mixing. Based on previous models by [Lewis \(1969\)](#), [Carlson et al. \(1988\)](#), [Lumine et al. \(1989\)](#) and [Marley et al. \(1999\)](#), [Ackerman & Marley \(2001\)](#) proposed a new method to estimate the mixing ratio and vertical size distribution of cloud particles (A-M model hereafter). In the A-M model, the sedimentation timescale is esti-

mated through cloud microphysics, taking into account the atmospheric gas kinetics and dynamical viscosity. The model assumes an equilibrium between upward turbulent mixing and sedimentation, where the turbulent mixing is derived from the eddy diffusion in the atmosphere. The key assumptions of the A-M model are as follows:

1. Clouds are distributed uniformly in the horizontal direction.
2. Condensable particles rain out at (super)saturation while maintaining a balance of the upward and downward drafts.
3. It does not consider the cloud cover variations caused by precipitation or the microphysics between different types of clouds.

The A-M model was originally proposed for giant exoplanets and brown dwarfs and was tested on Jupiter’s ammonia clouds, demonstrating that this approach is applicable to a broad range of temperatures and planetary types.

Another popular 1-D cloud microphysics model is the Community Aerosol and Radiation Model for Atmospheres (CARMA), initially developed for the Earth’s stratospheric sulfate aerosols (Turco et al. 1979; Toon et al. 1979). CARMA is a time-dependent cloud microphysics model which solves the discretised continuity equations for aerosol particles starting from nucleation. Gao et al. (2018) extended the use of CARMA to simulate clouds on giant exoplanets and brown dwarfs by including additional condensates predicted to form in hot atmospheres and compared the results with the A-M model. The A-M model, while able to provide the cloud particle sizes and number density distributions, is of intermediate numerical complexity and, therefore, potentially adaptable to be included in retrieval codes. In addition to the original implementation by Ackerman & Marley (2001), Virga (Rooney et al. 2022) simulates the cloud’s particle size distribution from the A-M approach and estimates separately the sedimentation efficiency. PICASO (Robbins-Blanch et al. 2022; Batalha et al. 2019) adopts Virga to simulate cloudy exoplanetary atmospheres. Adams et al. (2022) couples MIT GCM and Virga to include clouds in 3-D models. Xuan et al. (2022) present high-resolution spectroscopic simulations with petitTRANS (Mollière, P. et al. 2020). There, clouds are modelled from the A-M theory and spectra are simulated with Mie theory and DHS. None of these models, however, are currently available for retrieval simulations.

To simulate inhomogeneities for cloud formation in the horizontal direction, we would need to consider global circulation atmospheric effects, such as those modelled in Cho et al. (2021). An example of 3-D atmospheric model with clouds is Aura-3D (Welbanks & Madhusudhan 2021; Nixon & Madhusudhan 2022). The retrieval part for Aura-3D is highly parametrised, both for the atmospheric and cloud parameters. Helling et al. (2022, 2019) have simulated global cloud distributions by generating inputs to their kinetic cloud model from pre-calculated 3D Global Circulation Models (GCMs). Unfortunately, these complex models require excessive computing time. In addition, the data expected to be observed in the near future are unlikely to constrain the large number of parameters needed in a 3-D model. Therefore, while theoretical studies with 3-D models are very important to progress in our understanding of clouds in exoplanetary atmospheres and as benchmarks, they are currently less useful for interpreting available data.

In this paper, we present a new cloud retrieval model, *YunMa*, optimised for transit spectroscopy. In *YunMa*, we built the cloud model based on Ackerman & Marley (2001) and simulated the cloud contribution to transit spectra using extinction coefficients as calculated by the open-source B-H Mie code (Bohren & Huffman 2008). *YunMa* is fully integrated into the *TauREx 3* retrieval platform (Al-Refaie et al. 2022; Al-Refaie et al. 2021; Al-Refaie et al. 2019) and, for the first time, provides cloud microphysics capabilities into a retrieval model. We describe the model in Section 2. In Section 3, we detail the experimental setups. In Section 4, we validate particle size distributions and spectroscopic simulations against previous studies published in the literature. After validation, we show new spectral and retrieval simulations obtained with *YunMa*. In Section 5, we discuss our results and assumptions and identify possible improvements to the model to be considered in future developments.

2. MODEL DESCRIPTION

YunMa estimates the vertical distribution of the cloud particle sizes (VDCP hereafter, see, e.g. Fig. B1 b and B4 a, b in Appendix B) based on A-M model and their contribution to the radiative transfer calculations. The *YunMa* module has been integrated into the *TauREx 3* retrieval platform: the combined *YunMa-TauREx* model is able to constrain the VDCP from observed atmospheric spectra, as described in detail below.

2.1. Modelling the cloud particle size distribution

YunMa model contains a numerical realisation of the A-M microphysical approach to simulate the VDCP. We

show in Fig. 1 a pictorial representation of the A-M approach: it assumes that clouds form with different VDCP to maintain the balance between the upward turbulent mixing and downward sedimentation of the condensable species. Depending on the atmospheric T - p profile, multiple cloud layers may form.

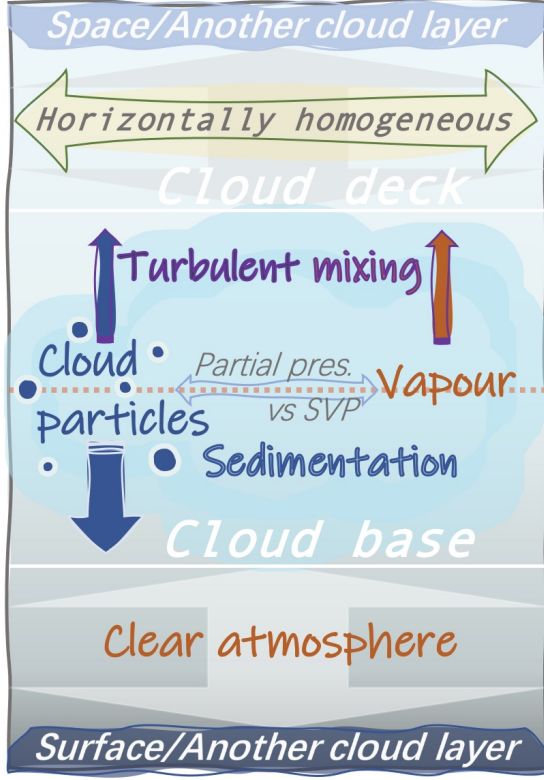


Figure 1. Sketch of the A-M micophysical approach adopted in *YunMa*. Cloud particles may form when the mixing ratio of the condensable gas exceeds the saturation mixing ratio, which is derived from its saturation vapour pressure (SVP). The vertical distribution of the cloud particle sizes (VDCP) is derived from the balance between the sedimentation of the cloud particles and the atmospheric turbulent mixing.

2.1.1. Cloud mixing profile

Cloud particles start forming when the partial pressure of a certain gas exceeds the saturation vapour pressure (SVP); the formation strongly depends on the atmospheric thermal structure. The condensation process, occurring when the partial pressure exceeds the SVP, is estimated by comparing the molecular mixing ratio of the gas phase with its saturation vapour mixing ratio:

$$q_c(z) = \max[0, q_t(z) - (S_c + 1) q_s(z)], \quad (1)$$

where q_c is the mixing ratio of the condensed species, z is the altitude, q_s is the mixing ratio where the con-

densable gas saturates, q_t is the total mixing ratio of a condensable chemical species, including both the condensate and gas phases, and S_c is the supersaturation factor which persists after condensation. q_s can be estimated from the ratio between the SVP of a certain chemical species and the atmospheric pressure at the same altitude. Note that in this paper, the mixing ratio refers to the volume fraction of a chemical species in the atmosphere.

In the A-M approach, the turbulent mixing of the condensate and vapour is assumed to be in equilibrium with the sedimentation of the condensate:

$$-K(z) \frac{\partial q_t(z)}{\partial z} - f_{\text{sed}} w_*(z) q_c(z) = 0, \quad (2)$$

where K ($\text{m}^2 \text{s}^{-1}$) represents the vertical eddy diffusion coefficient, and w_* (m s^{-1}) is the convective velocity. f_{sed} is the ratio between the mass-weighted droplet sedimentation velocity and w_* , defined as:

$$f_{\text{sed}} = \frac{\int_0^\infty v_f \frac{dm}{dr} dr}{\varepsilon \rho_a w_* q_c}; \quad (3)$$

here ρ_a is the atmospheric mass density, which can be estimated through the Ideal Gas Law, ρ_p is the mass density of a condensed particle, ε is the ratio between the molecular weights of the condensates and the atmosphere, and v_f is the sedimentation velocity which will be explained later. The first term in equation (2) describes the upward vertical draft derived from the macroscopic eddy diffusion equation. The second term describes the downward sedimentation, which is in equilibrium with the first term.

The eddy diffusion coefficient (K) is one of the key parameters affecting cloud formation. In free convection (Gierasch & Conrath 1985), it can be estimated as:

$$K = \frac{H}{3} \left(\frac{L}{H} \right)^{\frac{4}{3}} \left(\frac{RF}{\mu \rho_a c_p} \right)^{\frac{1}{3}}, \quad (4)$$

where H , μ and c_p are, respectively, the atmospheric scale height, mean molecular weight and specific heat capacity. $F = \sigma T_{\text{eff}}^4$ is the approximated radiative flux. The turbulent mixing length (L) is the scale height of the local stability in eddy diffusion, as opposed to the atmospheric scale height (H). In *YunMa*, we use the value of K as estimated by the atmospheric chemistry models embedded in *TauREx 3* (Al-Refaie et al. 2022; Al-Refaie et al. 2021) and derive L , accordingly, from equation (4). The convective velocity scale (w_*) mentioned above can also be estimated as a ratio between K and L .

The sedimentation velocity, denoted by v_f , is the speed at which a cloud particle settles within a heterogeneous mixture due to the force of gravity. v_f can be

estimated through viscous fluid physics:

$$v_f = \frac{2}{9} \frac{\beta g r^2 \Delta \rho}{\eta}, \quad (5)$$

where $\Delta \rho$ is the difference between ρ_p and ρ_a , β is the Cunningham slip factor, and η is the atmospheric dynamical viscosity (See Appendix A for more details of SVP, β and η).

2.1.2. Particle size and number density

Following the A-M approach, we assume spherical cloud particles with radii r . The particle radius at w_* , denoted as r_w , can be obtained using these relationships between v_f and w_* :

$$v_f(r_w) = w_*, \quad (6)$$

and

$$v_f = w_* \left(\frac{r}{r_w} \right)^\alpha, \quad (7)$$

where α corresponds to the sedimentation velocity decrease in viscous flows. In A-M, the particle size distribution was constrained by in-situ measurements of Californian stratocumulus clouds, which followed a broad lognormal distribution. The assumption of lognormal distribution allows estimating the geometric mean radius (r_g), the effective radius (r_{eff}) and the total cloud particle number density (N), using the detailed definitions and derivations listed in Appendix A.

2.2. Cloud contribution in transit spectra

To estimate the wavelength-dependent cloud contribution to transit spectra, *YunMa* adopts the scattering theory and absorption cross sections as described in [Bohren & Huffman \(2008, BH-Mie hereafter\)](#), assuming spherical cloud particles. The cross-section of the cloud particles (k_λ) at each wavelength (λ) and particle size are estimated through the extinction coefficient (Q_{ext}) of the corresponding wavelength and particle size, derived by BH-Mie from the refractive indices of the cloud particles:

$$k_\lambda = Q_{\text{ext}} \pi r^2. \quad (8)$$

We used the water ice refractive indices reported in [Warren & Brandt \(2008\)](#) for our simulations of the temperate super-Earth. We show some examples of atmospheres with water ice clouds in Section 4. Post-experimental tests were conducted to avoid the contamination of liquid water particles.

We simulate the cloud optical depths from the particle sizes and number densities along each optical path, which passes the terminator at altitude z_{ter} , with a path length $s_{z_{\text{ter}}}$ of each atmospheric layer:

$$\tau_\lambda = \int_{z_{\text{ter}}}^{z_{\text{top}}} \int_0^\infty k_\lambda \frac{dn}{dr} dr \frac{ds_{z_{\text{ter}}}}{dz} dz, \quad (9)$$

where n is the accumulated number density of particles with a radius smaller than r and z_{top} is the altitude at the top of the atmosphere. The contribution of the clouds to the transit spectra, ΔF_c , can be estimated as:

$$\Delta F_c = \frac{2 \int_{z_{\text{bottom}}}^{z_{\text{top}}} (R_p + z)(1 - e^{-\tau_\lambda}) dz}{R_s^2}, \quad (10)$$

where z_{bottom} is the altitude at R_p . While *YunMa* has the capability to include any customised cloud particle size distribution in the spectral simulations, in this paper, we aim at model testing and, for simplicity, we use a single radius bin, i.e. uniform cloud particle size $r_c = r_g$ (see equation A5 in Appendix A) for each atmospheric layer in the radiative-transfer simulation.

2.3. YunMa-TauREx: retrieval of cloudy atmospheres

We integrate the *YunMa* VDCP and τ_λ simulations in the Tau Retrieval of Exoplanets framework (*TauREx 3*, [Al-Refaie et al. 2022](#); [Al-Refaie et al. 2021](#); [Al-Refaie et al. 2019](#)), which allows atmospheric retrieval simulations. *TauREx 3* combined to *YunMa* allow us to perform retrievals which include cloud microphysical processes and cloud scattering properties. Parameters estimated by *TauREx 3* include atmospheric T - p and chemical profiles, planetary (e.g., mass and radius) and stellar (e.g., temperature and metallicity) parameters. The radiative transfer calculations executed by *TauREx 3* consider molecular and atomic absorptions, Rayleigh scattering and collisionally induced absorptions (CIA) of H_2 - H_2 and H_2 - He pairs from [Cox \(2015\)](#).

YunMa uses as initial condition the gas mixing ratio profiles provided by *TauREx 3* chemistry models (q_t , equation 1, 2). In this paper, for simplicity, we assume the baseline chemical abundances are constant with altitude instead of a more complex chemical structure. *YunMa* then adjusts the gas phase mixing ratios, atmospheric mean molecular weight and atmospheric density in the *TauREx 3* chemistry models as a result of the formation of clouds. To simulate transit spectra and perform retrievals, we use the atmospheric grids and optical paths defined in *TauREx 3* and add the cloud opacities as estimated by *YunMa* B-H Mie to the absorptions caused by the chemical species, using the methods explained in Section 2.2. The retrievals were tested on 80 Intel(R) Xeon(R) Gold 6248 CPU @ 2.50GHz.

3. METHODOLOGY

In this paper, we use *YunMa* to perform retrieval simulations of small temperate planets, where we expect a considerable amount of H_2O to be present in the atmosphere. For simplicity, we consider only water clouds

Table 1. Priors for spectral retrieval experiments using *YunMa* of all the cases listed in Table 3.

Parameter	Unit	Ground	Mode	Priors
R_p	$\mathcal{R}_{J_e}^N$	0.20	factor	0.75 – 1.25
f_{sed}	...	Table 3	log	10^{-3} – 10^2
$X_{\text{H}_2\text{O}}$...	Table 3	log	10^{-12} – 1
p_c	bar	Table 3	log	10^{-4} – 1
T_c	K	200	linear	0 – 500
T_{surf}	K	1000	linear	500 – 2000
X_{N_2}	...	Table 3	linear	10^{-12} – 1

NOTE— $X_{\text{H}_2\text{O}}$ represents the water vapour mixing ratio

forming in the atmosphere and we do not consider super-saturation cases. The planetary parameters are inspired by K2-18 b (Tsiaras et al. 2019; Charnay et al. 2021 b; Yu et al. 2021), which is a suitable candidate for cloud model testing. We list all the priors of our experiment in Table 1. In this work, we set K as a constant and estimate η using the approximation proposed by Rosner (2012, equation A4). We include both scattering and absorption due to water clouds based on Bohren & Huffman (2008), Rayleigh scattering of all the gas species and CIA of $\text{H}_2\text{-H}_2$ and $\text{H}_2\text{-He}$ pairs, which are enabled by *TauREx 3*. We fine-tune the abundance of N_2 to adjust the scale heights of the atmosphere. H_2 and He act as the filling gases. We use the POKAZATEL dataset for $^1\text{H}_2^{16}\text{O}$ (Polyansky et al. 2018) from the ExoMol database¹ (Tennyson & Yurchenko 2012; Tennyson & Yurchenko 2021; Chubb et al. 2021) to estimate the water vapour absorption and Rayleigh scattering. The CIA data is from HITRAN² (Karman et al. 2019). We use the PHOENIX library (Husser et al. 2013) to simulate the stellar atmospheres spectra.

For the numerical parameter settings, after a number of tests, we decided to use the explicit Runge-Kutta method of order 8 (DOP853, Hairer et al. 1988) with relative tolerance (*rtol*) of 1×10^{-13} and absolute tolerance (*atol*) of 1×10^{-16} to solve the partial differential equation (2) for all the experiments presented in Section 4. We have opted for a logarithm sampling to retrieve most of the atmospheric parameters, e.g., f_{sed} , $X_{\text{H}_2\text{O}}$ and p_c . We have used a linear sampling, instead, for N_2 to obtain a better numerical performance. The priors are sufficiently unconstrained to avoid biases generated by excessive pre-knowledge, as discussed, e.g. in

Changeat et al. (2021a). After a number of tests, we have chosen to use 400 live points for 3-dimensional retrievals and 1000 for more dimensions.

To begin with, we run a sensitivity study with *YunMa* about the planetary and instrumental parameters. We set the planetary radius (R_p), f_{sed} and $X_{\text{H}_2\text{O}}$ as free parameters in our 3-dimensional retrieval tests. We list in Table 1 the planetary parameters adopted in the simulations, the prior ranges and the sampling modes. The simulations are conducted with 80 atmospheric layers, from 10 bar to 10^{-6} bar, which encompass the typical observable atmospheric range for super-Earths. We select Case 2 in Table 3 as the nominal case, and test the model sensitivity to the key parameters in the retrievals. In Case 2, clouds dampen the gas spectroscopic features but do not obscure them entirely (see Fig. 3). The nominal f_{sed} refers to the value adopted in A-M. The water SVP (both liquid and ice) used are taken from Appendix A in A-M.

SENSITIVITY STUDIES TO KEY ATMOSPHERIC PARAMETERS

We have performed sensitivity studies to test how the model behaves when changing some of the key atmospheric parameters, including p_c , f_{sed} , $X_{\text{H}_2\text{O}}$, X_{N_2} (Case 1–9). Isothermal T - p profiles, as commonly used in transit retrieval studies, are too simplistic for cloud studies. We first assume T - p profiles with a dry adiabatic lapse rate in the troposphere, a moist adiabatic lapse rate in the cloud-forming region and a colder isothermal profile above the tropopause. To be compatible with the computing requirements in retrieval, we simplify it to a "two-point" profile (e.g., Fig. 5 in Section 4) in *TauREx* while keeping the lapse rate at the cloud deck, since the cloud formation is more sensitive to it than the T - p profile in the deeper atmosphere from our preliminary sensitivity tests. We define as T_c and p_c the temperature and pressure at the tropopause and T_{surf} the temperature at 10 bar. By tuning p_c , the altitude at which the cloud forms and the cloud's optical thickness will be altered. Here we test p_c from 10^{-3} to 10^{-1} bar (Case 1–5), which is a much broader range than the one considered in previous literature about K2-18 b. In Case 6, we set the sedimentation efficiency f_{sed} to 0.01, i.e. the downward sedimentation of the cloud particles is relatively slow compared to the net upward molecular mixing of the condensable species. By contrast, in Case 7 where $f_{\text{sed}} = 10$, we have a larger downward draft velocity scale compared to the upward one. In Case 8 and 9, we modulate the amount of condensable gas, here represented by the water vapour mixing ratio ($X_{\text{H}_2\text{O}}$).

¹ <https://exomol.com>

² <https://hitran.org>

SENSITIVITY STUDIES TO DATA QUALITY

The new generation of space-based facilities, such as JWST and Ariel, will deliver unprecedentedly high-quality data in terms of wavelength coverage, signal-to-noise ratio and spectral resolution. We select as nominal case transit spectra covering 0.4–14 μm , at a spectral resolution of 100, with 10 ppm uncertainty across wavelengths. We chose 0.4 μm as the blue cut-off to maximise the information content about Rayleigh scattering and 14 μm as the red cut-off to maximise the information content about water vapour and atmospheric temperature for the type of planets considered here. We then test how *YunMa*'s performances degrade when we compromise with any of those parameters, for instance: uncertainties of 30 ppm in Case 11 and spectral resolution of 10 in Case 12, which should have similar effects. We move the blue cut-off at longer wavelengths in Case 13.

RETRIEVALS OF ATMOSPHERIC THERMAL PROFILES

We have run retrieval experiments to test how *YunMa* performs with increasingly complex model assumptions and which parameters may be problematic in these retrievals. *YunMa*'s ability to retrieve p_c , T_c and T_{surf} were studied in Cases 14–17. In Case 15, we use a higher quality spectrum as input and compare the results with Case 14.

ADDITION OF N_2 IN RETRIEVALS

Inactive, featureless gases, such as N_2 , inject much uncertainty in the retrieval. In Cases 18–20, we include different amounts of the inert and featureless gas N_2 in the atmosphere. N_2 may exist in super-Earths' atmospheres, as it happens for Solar System planets at similar temperatures. Being N_2 heavier than H_2O , we adjust the mean molecular weight and the scale heights accordingly by modulating X_{N_2} . Heavier atmospheres have smaller scale heights: the spectral features are less prominent and harder to detect. We first try to retrieve only R_p , f_{sed} , X_{H_2O} and X_{N_2} .

DEGENERACY BETWEEN CLOUDS AND HEAVY ATMOSPHERE

In Cases 14–20, N_2 and the T - p profile were retrieved separately. Here we attempt to retrieve the cloud microphysics parameters (f_{sed}) together with X_{N_2} , the T - p profile and other atmospheric parameters. Case 21 retrieves these parameters except X_{N_2} fixed to 50% for comparison with Case 22 to investigate the degeneracy imposed by the uncertainty of X_{N_2} . In Case 22, we perform the full retrieval including both X_{N_2} and the T - p profile as free parameters. Similar to N_2 , decreases the

scale height and compresses the transit spectrum, the existence of clouds mitigates the spectral features, and the difference between these two scenarios may be difficult to distinguish from the current data quality. One hypothesis is that if we do not include N_2 among the priors, the model will add clouds to compensate for the missing N_2 . In Case 23, we test this hypothesis by forcing X_{N_2} to zero and then monitor the cloud parameters in the posteriors obtained.

COMPARISON OF CLOUD RETRIEVAL MODELS

Here forward spectra are simulated with *YunMa* cloud microphysics and then retrieved with another simplified cloud retrieval framework. In Case 24, clouds are described as an opaque cloud deck across wavelengths in *TauREx 3*, which is commonly used to retrieve data from the last decades with narrow wavelength coverage, e.g., HST/WFC3. In Case 25, we deliberately omit cloud parameters in the retrieval priors and learn if and how other parameters can compensate for those missing.

RETRIEVALS OF FEATURELESS SPECTRA

In Cases 26–28, we retrieve the atmospheric parameters from spectra with minimal spectroscopic features, where spectral standard deviation (σ_{spec}) is less than 1 ppm. The spectra are featureless due to heavy atmospheres and cloud contribution. In Case 28, we unrealistically decrease the uncertainty to 1 ppm at resolving power 100 to evaluate *YunMa*'s performance with idealised data quality.

4. RESULTS

4.1. Model validation

We validated our model against [Ackerman & Marley \(2001\)](#) by comparing the condensate mixing ratios of Jovian ammonia clouds (q_c) with different values of f_{sed} , as shown in Fig. 2. The two sets of results are consistent and the small differences in q_c translate into $\sim 10^{-2}$ ppm in transit depth, which is completely negligible compared to typical observational noise.

We further validated our model against the results from [Gao et al. \(2018\)](#) by comparing the KCl cloud molecular mixing ratio and particle-size profile (see Fig. B1 in Appendix B). [Gao et al. \(2018\)](#) used CARMA to simulate cloud microphysics in exoplanets and brown dwarfs with $T_{\text{eff}} = 400$ K and $\log g = 3.25, 4.25$ and 5.25 (in cgs units), corresponding to planetary masses of 0.72 M_J , 8.47 M_J , and 44.54 M_J . In the best fit between CARMA to A-M model, the $f_{\text{sed}} = 0.125, 0.093$ and 0.025 for the cases with $K = 10^4, 10^3$ and 10^2 $\text{m}^2 \text{s}^{-1}$, respectively. The mixing length is derived from constant eddy diffusion, as described in equation (4). The

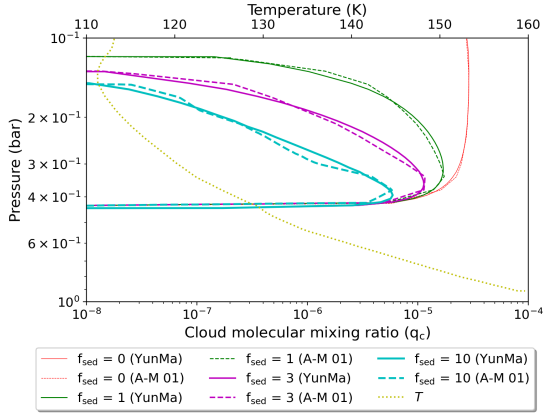


Figure 2. Validation of the *YunMa* cloud microphysics model against the Jovian ammonia clouds in Ackerman & Marley (2001). q_c corresponding to different sedimentation efficiencies (f_{sed}) are shown. Solid lines: results from *YunMa*. Dashed lines: results from Fig. 1 in Ackerman & Marley (2001). Dotted line: T - p profile.

results agree with each other within 8 %, i.e. $\sim 10^{-3}$ ppm difference in the transit depth.

We compared simulations from *YunMa* with the results from Charnay et al. (2021 b, see Fig. B2 in Appendix B), which include the horizontal effects generated by global circulation. Being *YunMa* a 1D model, we cannot reproduce the exact same results, but we can have an approximated comparison with their simulations at the substellar point, where the horizontal winds are weak. We assume $100 \times$ solar composition, with $f_{\text{sed}} = 3$ and $K = 10^6 \text{ cm}^2\text{s}^{-1}$. Both models predict clouds forming in the region between 3×10^{-2} and 1×10^{-2} bar and a cloud molecular mixing ratio $\sim 10^{-4}$.

We have validated the BH-Mie module in *YunMa* against PyMieScatt, an open-source model simulating atmospheric particle scattering properties (Sumlin et al. 2018), as shown in Fig. B3. Cloud particle radii were selected in the range of 0.1-100 μm . The largest discrepancy in Q_{ext} is within ± 0.002 , which corresponds to an average of 0.01 ppm in the planetary transit depth of the nominal scenario in our experiments.

4.2. Simulated transit spectra with *YunMa*

We present here the transmission spectra generated with *YunMa* of a cloudy super-Earth. Fig. 3 shows five examples at resolving power of 100 which corresponds to the ground truths of some of the retrieval cases in Table 3: $p_c = 2 \times 10^{-3}$ bar with $X_{\text{N}_2} = 0$ (blue, Case 2, 10, 11, 14 and 15) and $= 0.5$ (purple, Case 20–25); $p_c = 1 \times 10^{-2}$ bar with $X_{\text{N}_2} = 0$ (green, Case 3 and 16) and $= 0.5$ (yellow, Case 27 and 28) and one case of opaque cloud with $p_c = 1 \times 10^{-2}$ bar in the H_2/He dominated atmosphere (red, Case 4 and 17). The plan-

etary and atmospheric parameters are listed in Table 1 and 3. All the simulations contain baseline 10% H_2O abundance across the atmosphere, which is then altered by the cloud formation. The rest of the atmosphere is N_2 and H_2/He . We select $f_{\text{sed}} = 3$ for all the scenarios. The simulation results are summarised in Table 2.

In the experiment without N_2 and p_c set to 2×10^{-3} bar, clouds form at high altitude, where the atmospheric density (ρ_a) is low compared to the cases where $p_c = 5 \times 10^{-3}$ bar and $= 1 \times 10^{-2}$ bar. Here the sedimentation velocity (v_f) is small with small cloud particle radii and number density. The cloud contribution (blue dash-dotted line) has a mean transit depth of 2660 ppm and σ_{spec} of 17 ppm. It is an optically thin cloud which does not completely block the spectral features shaped by water vapour absorption (blue dotted line). When $p_c = 1 \times 10^{-2}$ bar, clouds form at relatively low altitudes, where the atmospheric density (ρ_a) is high. Here v_f is large and the cloud particles have relatively large radii and number density, which increase the opacity. The cloud contribution (red dash-dotted line) has a mean flux depth of 2727 ppm and σ_{spec} of 0.62 ppm. Since the clouds are optically thick, they contribute significantly to the mean transit depth and obscure the spectral features of water vapour (red dotted line). However, the water vapour features are still able to show due to the low altitude of the clouds. Still, the spectral deviation is only 12.16 ppm, where the spectroscopic features have a high chance of being hidden by the observational uncertainty. $p_c = 5 \times 10^{-3}$ bar is an intermediate case regarding the simulated cloud altitude and opacity. The simulation suggests that the intermediate combination of these two cloud properties does not result in more significant atmospheric features than in other cases.

In atmospheres with relatively high mean molecular weight – and therefore small scale height – for the same value of p_c , the transit depth is smaller, as expected. In the case with $X_{\text{N}_2} = 0.5$ and $p_c = 2 \times 10^{-2}$ and $= 5 \times 10^{-2}$ bar, the mean value of the transit depths are ~ 200 ppm smaller than them in a H_2/He dominated atmosphere. Here the cloud particles form at higher ρ_a and therefore have larger particle size and larger number density compared to those formed in the H_2/He dominated atmospheres. The spectrum has σ_{spec} of 2.58 and 0.62 ppm, which are negligible compared to the observational uncertainty.

Besides p_c and X_{N_2} , we also have tested different f_{sed} to understand how this parameter controls the cloud microphysics. The particle radii, r_c , number density and transit spectra across all the cloud pressure levels and

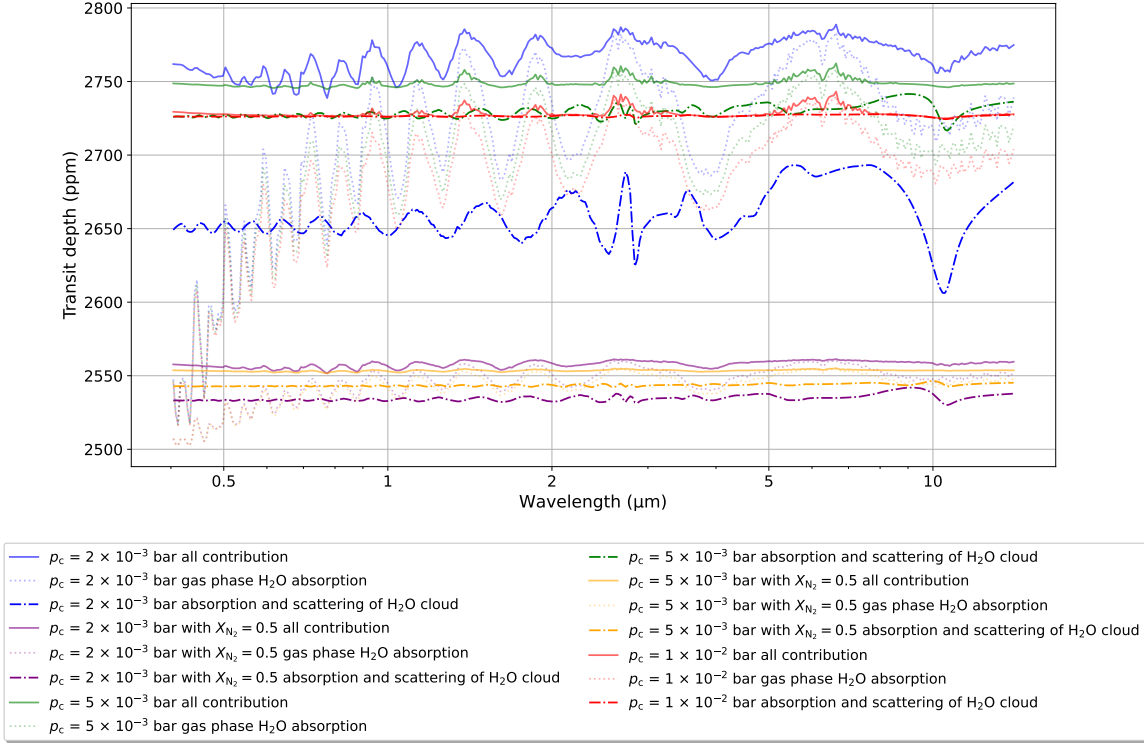


Figure 3. Simulated transit spectra of cloudy super-Earths using *YunMa*. Solid line: total transit depth with all contributions included; dot-dashed line: water ice clouds; faint-dotted line: water vapour. Blue, green and red lines: H_2/He dominated, cloudy atmospheres with different p_c (see legend). Purple and yellow lines: heavier cloudy atmospheres with 50% N_2 .

obtained with different f_{sed} are shown in Fig. B4. Here we note that, from the results, the cloud particle sizes increase with f_{sed} while the number densities at each layer behave reversely. Also, which is easy to understand, the more atmospheric layers with clouds, the larger the optical depth.

4.3. Retrieval results

We show in this section how *YunMa* performs with different model assumptions and ground truth parameters (GTPs), following the approach described in Section 3. GTPs and priors are listed in Table 1. The posterior median values and their standard deviations obtained for all the simulated cases are summarised in Table 3.

Cases 1–5 test the effects of different p_c to the transit spectra and retrievals. The transit spectra of Cases 2 and 4 are shown in Fig. 3 (blue and red solid lines respectively). The larger is p_c , the more opaque meanwhile, the lower altitude becomes the clouds. The significance of spectroscopic features owns to both factors, and generally speaking, the more significant features are, the easier it is to retrieve the atmospheric parameters. We choose $p_c = 2 \times 10^{-3}$ bar as nominal case and show the corresponding posterior distributions in Fig. 4. Cases 2, 6 and 7 test the impact on the transit spec-

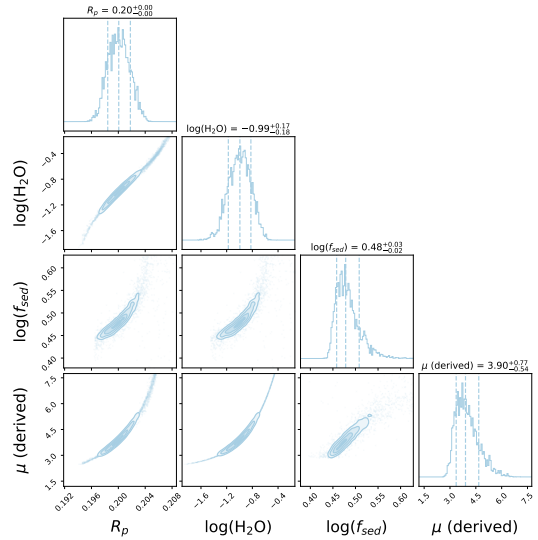


Figure 4. Example of cloud retrieval using *YunMa* integrated in *TauREx 3* (Case 2 in Table 3). The sedimentation efficiency (f_{sed}), which is the main parameter controlling the cloud microphysics, is well recovered together with the vapour water mixing ratio.

tra and retrievals of the sedimentation efficiency (f_{sed}), which controls the cloud microphysics in our model. In all three cases, GTPs for f_{sed} , $X_{\text{H}_2\text{O}}$ and R_p are well

Table 2. Atmospheric and cloud parameters included in *YunMa* simulations. The corresponding transit depths are also reported.

		p_c	2×10^{-3} (bar)	5×10^{-3} (bar)	1×10^{-2} (bar)	2×10^{-3} (bar)	5×10^{-3} (bar)
	X_{N_2}	0.5	0.5
Parameter	Unit						
All contribution, mean	ppm	2770.17		2750	2729.82	2558.65	2553.71
All contribution, std (σ_{spec})	ppm	15.72		11.59	12.16	2.58	0.62
Cloud contribution, mean	ppm	2659.65		2729.60	2726.53	2534.78	2542.78
Cloud contribution, std	ppm	17.21		4.39	0.62	2.15	0.85
MMW (bottom of the atmosphere)	g mol^{-1}	3.88		3.88	3.88	16.73	16.73
Atmospheric pressure (cloud base)	bar	2.34×10^{-3}	6.40×10^{-3}	2.34×10^{-3}	1.43×10^{-2}	2.34×10^{-3}	6.40×10^{-3}
Atmospheric pressure (cloud deck)	bar	8.54×10^{-4}	2.34×10^{-3}	2.34×10^{-3}	4.28×10^{-3}	8.54×10^{-4}	2.33×10^{-3}
Cloud MMR (cloud base)	...	6.35×10^{-4}	9.51×10^{-5}	9.51×10^{-5}	2.00×10^{-4}	2.92×10^{-4}	4.35×10^{-4}
Cloud MMR (cloud deck)	...	7.56×10^{-8}	2.92×10^{-7}	2.92×10^{-7}	7.28×10^{-8}	3.49×10^{-7}	1.33×10^{-6}
v_f	m s^{-1}	6.54 – 7.53	6.07 – 6.67	6.07 – 6.67	4.43 – 6.41	7.14 – 7.97	4.37 – 7.28
r_c	μm	9.03 – 6.39	9.79 – 8.88	9.79 – 8.88	12.13 – 9.35	13.99 – 11.09	25.53 – 13.66
N (cloud base)	m^{-3}	1.03×10^4	3.19×10^4	3.19×10^4	7.47×10^4	1.28×10^4	8.22×10^3
N (cloud deck)	m^{-3}	1.45×10^1	5.72×10^1	5.72×10^1	2.24×10^1	1.28×10^1	7.16×10^1

NOTE—MMR and MMW: molecular mixing ratio and mean molecular weight. The pressure at the bottom of the atmosphere is assumed to be 10 bar.

within the retrieved parameter space, with more or less peaked and symmetric posterior distributions. When $f_{\text{sed}} = 0.01$ and 3, the posterior distributions of f_{sed} are closer to normal distribution centred at the retrieved solution. When $f_{\text{sed}} = 10$, the upper limit is not well constrained in the posterior distribution of f_{sed} . This effect is not unexpected, as high f_{sed} scenarios tend to have negligible impact on the planetary transit depth due to thinner cloud layers and smaller number density (N) compares to a low f_{sed} scenario, e.g., the $f_{\text{sed}} = 10$ and 100 cases in Fig. B4. From the experiments on the baseline water abundance ($X_{\text{H}_2\text{O}}$), in atmospheres where water can condense, when the $X_{\text{H}_2\text{O}}$ is less than 1×10^{-3} , clouds cannot form. When $X_{\text{H}_2\text{O}} = 0.01$ (Case 8) a thin cloud with low opacity may form, the water vapour spectral features are well visible and the retrieval performs well. By contrast, a higher mixing ratio of the condensable gas increases the partial pressure and contributes to the condensation process. This is, for instance, the case of $X_{\text{H}_2\text{O}} = 0.5$ (Case 9) where the cloud is thick and largely blocks the spectral features, making the retrieval of the atmospheric parameters difficult.

From the experiments on observational data quality, Case 10’s Bayesian evidence (4568.52) compared to the ones calculated for Case 2 (3755.80) and Case 11 (3368.29) showcases how the retrieval performance improves when the observational uncertainties are small. Case 12 performs better than Case 2, as the spectral resolution of the transit spectrum used as input to the retrieval is higher. In Case 13, we omitted the informa-

tion contained in the optical wavelengths, which means that we have less information about the cloud scattering properties. The retrieval performances are degraded compared to Case 2, which includes the optical wavelengths.

In Case 14–17, we retrieved the T - p profiles as free parameters for different p_c . Our results show that both the T - p profiles and cloud parameters can be constrained, although the retrieved gas phase mixing ratio and f_{sed} have large standard deviations. Case 18 compared to Case 2 showcases how the addition of the spectrally inactive N_2 injects uncertainty in the retrieval. Different amounts of N_2 (X_{N_2}), are considered in Cases 18–20. Despite the minimal spectral features of the cloudy heavy atmospheres due to N_2 injection, it is still able to retrieve the atmospheric parameters in simple cases.

In Cases 21–25 we retrieve both the T - p profile and X_{N_2} . The corresponding transit spectra are shown in Fig. 3 (purple lines). Case 21 shows how the atmospheric parameters, with the exception of X_{N_2} , can be retrieved in a heavy atmosphere with $X_{\text{N}_2} = 0.5$. When we include the uncertainty of X_{N_2} (Case 22), the GTPs for R_p , $X_{\text{H}_2\text{O}}$, f_{sed} , T_{surf} and T_{top} (see the retrieved T - p profile in Fig. 5) still fall into the 2σ confidence range. f_{sed} is significantly less constrained in Case 22 than Case 21 due to the uncertainty of X_{N_2} . Cases 22–24 are compared with each other in Fig. 6. Potential degeneracy could happen according to Case 23: when we omit N_2 among the priors, the retrieval tries to compensate for the missing radiative-inactive gas by

decreasing R_p and T_{surf} , while increasing $X_{\text{H}_2\text{O}}$, and the Bayesian evidence of Case 23 (3757.08) is close to Case 22 (3757.40). In the experiment of model comparison, if we use the simple opaque cloud retrieval model in *Tau-REx 3* (Case 24) instead of *YunMa* for the not opaque case, the cloud and other atmospheric parameters are significantly more degenerated and less constrained than using *YunMa*. Without the cloud in the prior (Case 25), the results show a lack of constraints on the T - p profile while comparable performance on other parameters with Case 22.

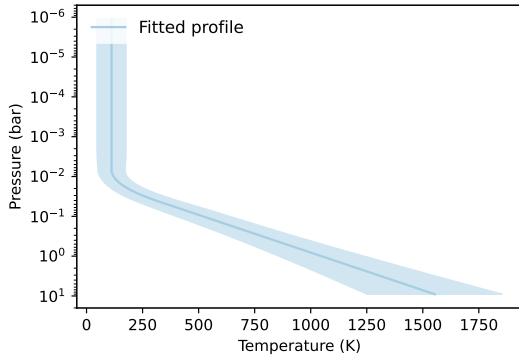


Figure 5. Retrieved T - p profile of Case 22 in Table 3. The isothermal temperature (T_c), surface temperature (T_{surf}) and the pressure where the isothermal profile starts (p_c) are retrieved using *YunMa*. The shaded area indicates the standard deviation of the posterior distribution.

Cases 26–28 focus on retrieval of plain spectra ($p_c = 5 \times 10^{-2}$ bar in a heavy atmosphere). The transit spectrum for Case 27 and 28 is shown in Fig. 3, yellow line: the spectral signal is very small compared to the observational uncertainty (10 ppm). As expected, the retrieval performance is limited unless the observational uncertainty is unrealistically decreased to 1 ppm (Fig. 7).

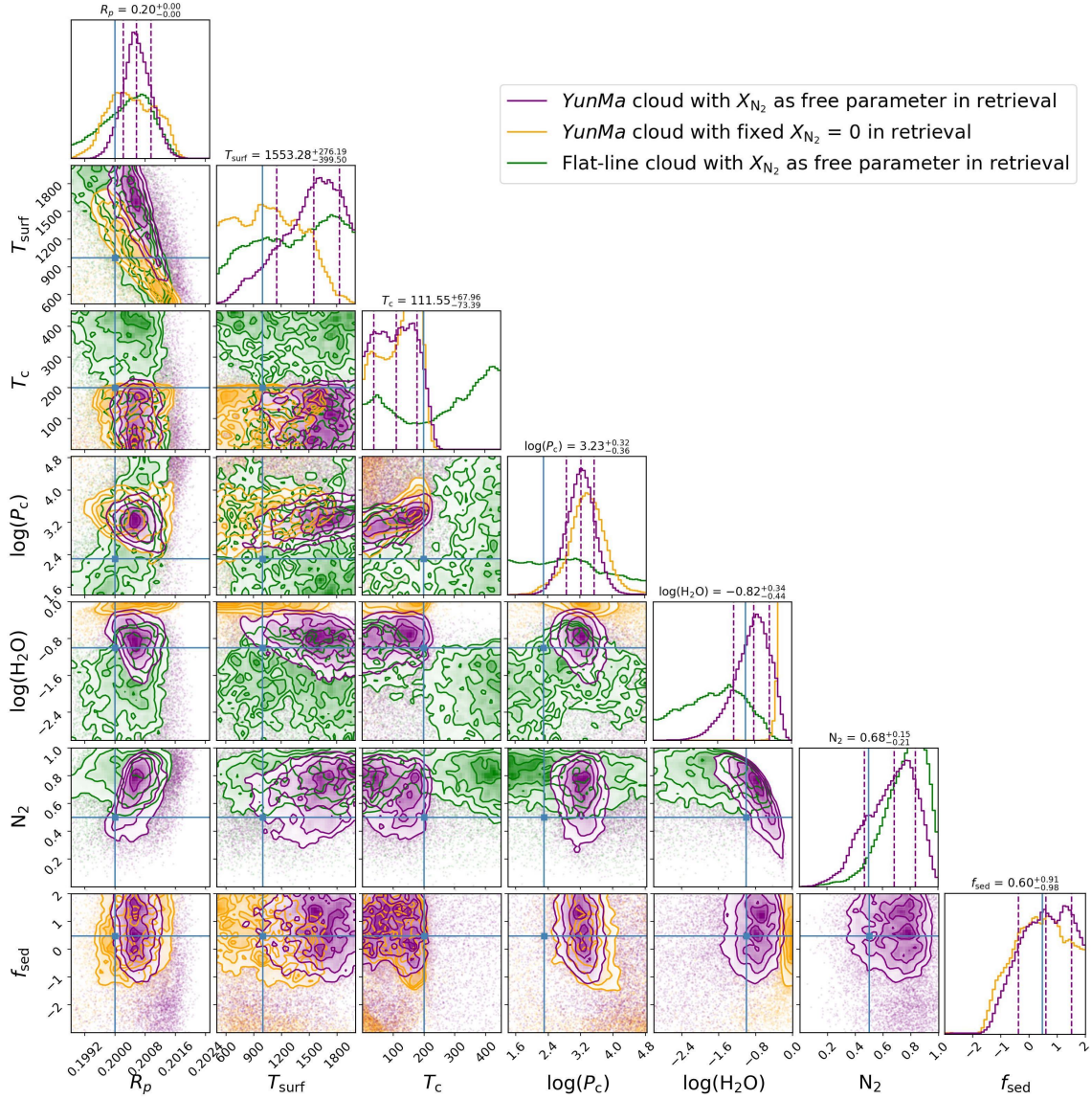


Figure 6. Retrieval posteriors for Case 22 (purple), 23 (orange) and 24 (green) in Table 3. Blue crosses indicate the ground truth parameters and the vertical dashed lines in histograms indicate the 1σ and 2σ confidence ranges of the posterior distribution. These three retrievals use the same transit spectrum as input (thin cloud with $X_{N_2} = 0.5$ in Fig. 3) but different retrieval assumptions. Case 22 (purple): H_2O and N_2 are included as priors and the cloud formation is simulated by *YunMa*. Case 23 (orange): same as Case 22 except that N_2 is not included among the priors. Case 24 (green): same as Case 22 except that the cloud is simulated by a simpler model from *TauREx*, in which the atmosphere becomes opaque below the cloud deck. The only retrieved cloud parameter for the simpler model is the cloud deck pressure, which is not shown here for simplicity.

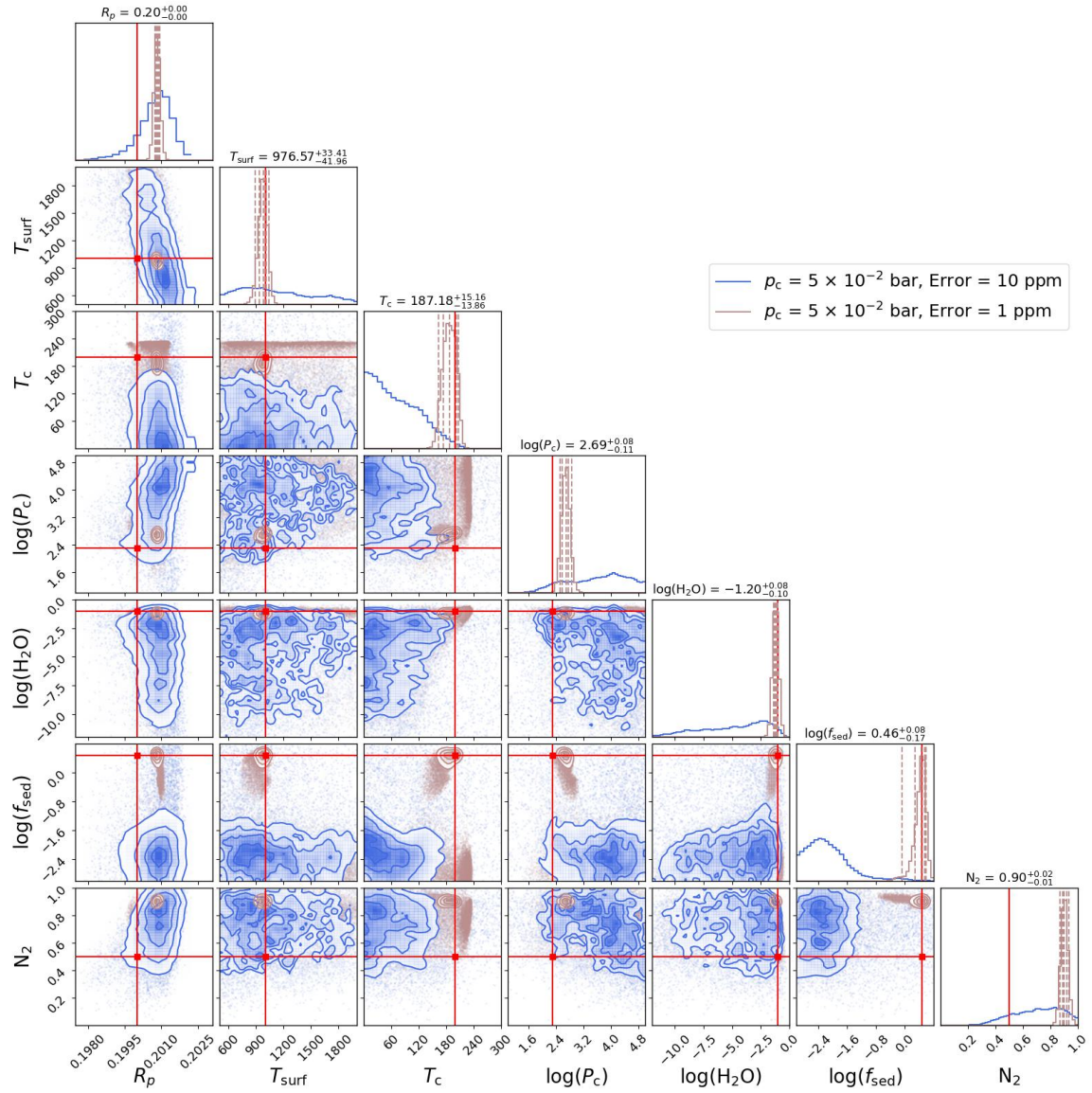


Figure 7. YunMa retrieval experiments with thick clouds and $X_{\text{N}_2} = 0.5$ (orange line in Fig. 3). Observational uncertainty = 10 ppm (blue line, Case 27 in Table 3) and = 1 ppm (brown line, Case 28 in Table 3). Red lines indicate GTPs.

Table 3. YunMa retrieval experimental results. The ground truth parameters (GTPs) assumed in the simulations are listed in the left columns of the table and the retrieved posteriors on the right. The retrieval priors are listed in Table 1. In each case, we test the model sensitivity of the atmospheric parameters of f_{sect} , p_c , $X_{\text{H}_2\text{O}}$, X_{N_2} , and the observational parameters of the error, wavelength coverage (λ) and the spectral resolution. We choose the nominal value of p_c as 2×10^{-3} bar, where the cloud is not either too thin to be detected or too thick to block the spectroscopic features.

Case	GTPs						Posteriors									
	$\log(f_{\text{sect}})$	$\log(p_c)$	$\log(X_{\text{H}_2\text{O}})$	X_{N_2}	Error (ppm)	λ (μm)	Res.	R_p	$\mathcal{R}_{\text{N}_2}^{\text{N}}$	$\log(f_{\text{sect}})$	$\log(X_{\text{H}_2\text{O}})$	X_{N_2}	$\log(p_c)$	T_c (K)	T_{surf} (K)	
1	0.48	-3	-1	...	10	0.4 - 14	100	$0.20^{+6.98e-06}_{-4.06e-06}$...	$0.29^{+0.00}_{-0.00}$	$-1.10^{+0.00}_{-0.00}$	
2	0.48	-2.7	-1	...	10	0.4 - 14	100	$0.20^{+1.72e-03}_{-1.64e-03}$...	$0.48^{+0.03}_{-0.02}$	$-0.99^{+0.17}_{-0.18}$	
3	0.48	-2.3	-1	...	10	0.4 - 14	100	$0.20^{+3.54e-03}_{-3.31e-03}$...	$-0.85^{+0.93}_{-1.56}$	$-1.34^{+0.47}_{-1.14}$	
4	0.48	-2	-1	...	10	0.4 - 14	100	$0.20^{+5.30e-03}_{-1.75e-03}$...	$-1.11^{+0.97}_{-0.75}$	$-1.57^{+0.79}_{-0.85}$	
5	0.48	-1	-1	...	10	0.4 - 14	100	$0.20^{+1.63e-03}_{-2.39e-03}$...	$-0.76^{+0.97}_{-0.81}$	$-1.22^{+0.31}_{-0.96}$	
6	-2	-2.7	-1	...	10	0.4 - 14	100	$0.20^{+2.80e-03}_{-1.19e-03}$...	$-2.02^{+0.09}_{-0.13}$	$-0.91^{+0.28}_{-0.62}$	
7	1	-2.7	-1	...	10	0.4 - 14	100	$0.20^{+7.09e-04}_{-2.50e-05}$...	$1.29^{+0.28}_{-0.01}$	$-0.92^{+0.07}_{-0.01}$	
8	0.48	-2.7	-2	...	10	0.4 - 14	100	$0.20^{+2.63e-05}_{-4.43e-03}$...	$0.44^{+0.00}_{-0.01}$	$-2.02^{+0.01}_{-0.01}$	
9	0.48	-2.7	-0.3	...	10	0.4 - 14	100	$0.20^{+4.43e-03}_{-3.44e-03}$...	$-1.22^{+1.06}_{-0.54}$	$-0.75^{+0.37}_{-0.37}$	
10	0.48	-2.7	-1	...	1	0.4 - 14	100	$0.20^{+1.62e-04}_{-1.63e-04}$...	$0.48^{+0.00}_{-0.00}$	$-1.00^{+0.02}_{-0.02}$	
11	0.48	-2.7	-1	...	30	0.4 - 14	100	$0.21^{+8.61e-04}_{-3.76e-03}$...	$0.77^{+0.85}_{-0.28}$	$-0.50^{+0.11}_{-0.37}$	
12	0.48	-2.7	-1	...	10	0.4 - 14	10	$0.21^{+7.33e-04}_{-2.85e-03}$...	$0.96^{+0.70}_{-0.44}$	$-0.47^{+0.10}_{-0.29}$	
13	0.48	-2.7	-1	...	10	1 - 14	100	$0.20^{+2.47e-03}_{-3.95e-04}$...	$0.51^{+0.10}_{-0.01}$	$-0.76^{+0.25}_{-0.04}$	
14	0.48	-2.7	-1	...	10	0.4 - 14	100	$0.20^{+7.53e-04}_{-9.24e-04}$...	$0.42^{+1.04}_{-1.15}$	$-0.62^{+0.07}_{-0.08}$...	$-2.39^{+0.35}_{-0.33}$	$124.55^{+56.56}_{-82.38}$	$1264.49^{+151.39}_{-121.10}$	
15	0.48	-2.7	-1	...	1	0.4 - 14	100	$0.20^{+1.39e-05}_{-1.44e-05}$...	$0.20^{+0.01}_{-0.02}$	$-0.71^{+0.00}_{-0.00}$...	$-2.54^{+0.02}_{-0.01}$	$194.23^{+4.14}_{-0.88}$	$1043.45^{+4.14}_{-1.91}$	
16	0.48	-2.3	-1	...	10	0.4 - 14	100	$0.21^{+7.71e-04}_{-1.02e-03}$...	$0.25^{+1.16}_{-1.24}$	$-0.09^{+0.06}_{-0.10}$...	$-1.21^{+0.52}_{-0.90}$	$175.25^{+31.87}_{-86.34}$	$1237.49^{+508.48}_{-528.66}$	
17	0.48	-2	-1	...	10	0.4 - 14	100	$0.20^{+6.24e-03}_{-2.88e-03}$...	$-1.84^{+2.65}_{-3.93}$	$-2.88^{+2.82}_{-3.93}$...	$-0.95^{+0.53}_{-1.03}$	$150.58^{+706.26}_{-122.39}$	$1000.70^{+4.76}_{-332.40}$	
18	0.48	-2.7	-1	10^{-12}	10	0.4 - 14	100	$0.21^{+2.88e-04}_{-1.72e-04}$...	$0.62^{+0.03}_{-0.02}$	$-0.86^{+0.12}_{-0.12}$	$0.11^{+0.03}_{-0.03}$	
19	0.48	-2.7	-1	0.1	10	0.4 - 14	100	$0.20^{+4.02e-04}_{-6.63e-04}$...	$0.67^{+0.59}_{-0.12}$	$-0.96^{+0.23}_{-0.24}$	$0.37^{+0.09}_{-0.07}$	
20	0.48	-2.7	-1	0.5	10	0.4 - 14	100	$0.20^{+1.82e-04}_{-2.84e-04}$...	$0.39^{+0.12}_{-0.10}$	$-1.03^{+0.33}_{-0.46}$	$0.74^{+0.13}_{-0.13}$	
21	0.48	-2.7	-1	0.5	10	0.4 - 14	100	$0.20^{+3.96e-04}_{-4.70e-04}$...	$0.56^{+0.96}_{-1.19}$	$-0.69^{+0.23}_{-0.33}$	fixed to 0.5	$-1.69^{+0.32}_{-0.36}$	$103.11^{+70.32}_{-69.47}$	$1443.65^{+373.77}_{-310.00}$	
22	0.48	-2.7	-1	0.5	10	0.4 - 14	100	$0.20^{+3.87e-04}_{-3.48e-04}$...	$0.60^{+0.91}_{-0.98}$	$-0.82^{+0.34}_{-0.44}$	$0.68^{+0.15}_{-0.21}$	$-1.77^{+0.32}_{-0.36}$	$111.53^{+67.82}_{-73.41}$	$1553.21^{+276.23}_{-399.58}$	
23	0.48	-2.7	-1	0.5	10	0.4 - 14	100	$0.20^{+7.03e-04}_{-6.06e-04}$...	$0.42^{+1.00}_{-1.02}$	$-0.11^{+0.07}_{-0.09}$	fixed to 0	$-1.62^{+0.42}_{-0.42}$	$130.80^{+52.94}_{-86.47}$	$1071.37^{+399.26}_{-381.53}$	
24	0.48	-2.7	-1	0.5	10	0.4 - 14	100	$0.20^{+6.13e-04}_{-9.64e-04}$	$-1.90^{+0.81}_{-1.36}$	$0.78^{+0.12}_{-0.18}$	$-2.27^{+1.22}_{-1.13}$	$327.32^{+120.86}_{-245.79}$	$1370.26^{+430.51}_{-535.90}$	
25	0.48	-2.7	-1	0.5	10	0.4 - 14	100	$0.20^{+3.80e-04}_{-3.47e-04}$	$-0.95^{+0.32}_{-0.47}$	$0.74^{+0.14}_{-0.16}$	$-1.72^{+0.38}_{-0.35}$	$48.60^{+51.83}_{-32.93}$	$1577.37^{+285.82}_{-401.02}$	
26	0.48	-2.3	-1	0.1	10	0.4 - 14	100	$0.21^{+4.38e-04}_{-8.41e-04}$...	$-2.27^{+0.67}_{-0.46}$	$-3.80^{+2.23}_{-3.28}$	$0.78^{+0.13}_{-0.18}$	$-1.31^{+0.82}_{-1.06}$	$86.15^{+65.71}_{-61.63}$	$1136.49^{+542.96}_{-444.41}$	
27	0.48	-2.3	-1	0.5	10	0.4 - 14	100	$0.20^{+4.50e-04}_{-6.77e-04}$...	$-2.20^{+0.60}_{-0.48}$	$-4.33^{+2.36}_{-3.92}$	$0.72^{+0.17}_{-0.21}$	$-1.29^{+0.80}_{-1.11}$	$62.56^{+65.77}_{-45.02}$	$1052.87^{+340.75}_{-342.32}$	
28	0.48	-2.3	-1	0.5	1	0.4 - 14	100	$0.20^{+4.47e-05}_{-4.72e-05}$...	$0.46^{+0.95}_{-0.17}$	$-1.20^{+0.08}_{-0.10}$	$0.90^{+0.02}_{-0.01}$	$-2.31^{+0.18}_{-0.11}$	$187.18^{+13.06}_{-13.88}$	$976.55^{+33.33}_{-41.97}$	

5. DISCUSSION

5.1. Transit spectroscopy using *YunMa*

To understand the performances of *YunMa* in detail, we performed retrieval experiments for over a hundred cases, with different chemistry models, atmospheric and cloud scenarios for super-Earths/sub-Neptunes, hot-Jupiters and brown dwarfs. A variety of cloud species were modelled and analysed. This paper presents a selection of representative examples. We have validated the A-M cloud size distribution in *YunMa* against previous literature simulating NH_3 clouds in Jupiter’s atmosphere, KCl clouds on artificial large exoplanets and brown dwarfs, and H_2O clouds on K2-18 b. We have also tested a number of numerical settings, including fitting methods, tolerances and retrieval samplings.

In *YunMa*, the mixing ratios of the condensable gas and the condensate are strongly correlated, therefore when cloud forms, the condensable species in the gas phase decreases. Also, a balance is imposed between the upward turbulent mixing and the downward sedimentation velocity from the A-M approach (equation 2). In the current *YunMa*, at each pressure level, the particle number density represents the total number density of particles with different radii. The Earth measurements shown in Fig. 4 of [Ackerman & Marley \(2001\)](#) suggest a bimodal distribution of the particle sizes at the same pressure level. *YunMa* is able to use radius bins with their respective number densities to represent more precisely the cloud distribution in the spectral simulation. For the retrieval calculations, however, we had to simplify this information to reduce the computing time.

The cloud opacity is determined by the cloud particle size and number density; different particle sizes have absorption and scattering peaks at different wavelengths. Optically thick clouds cause transit depths with negligible or no modulations as a function of wavelength: the atmosphere below the cloud deck is, in fact, undetectable while the atmosphere sounded above the cloud deck is more rarefied. Retrieving information about the atmospheric composition and structure is very difficult in the most extreme cases. For an atmosphere with optically thin clouds, the absorption features due to radiative-active gases (water vapour here) are detectable but less prominent compared with a clear atmosphere. The abundances of these gases can be retrieved largely from their absorption features. If these are condensable species, their abundances further constrain the cloud microphysics. Both the wavelength-dependent features and the overall transit depth help the retrieval performance.

f_{sed} is the ratio between the sedimentation velocity and the turbulent convective velocity. From the definition, a higher f_{sed} means a shorter sedimentation timescale, as we fixed K to a constant value. A higher sedimentation efficiency leads to larger offsets to the downward draft, constraining the upward supplement of water vapour and cloud formation. On the contrary, for small f_{sed} , the sedimentation timescale is much longer compared to the diffusion timescale, so the condensation continues at lower pressure to balance the downward sedimentation and upward turbulent mixing; therefore, the cloud region expands. f_{sed} is sensitive to the cloud particles’ nucleation rate ([Gao et al. 2018](#)). It has a close relationship with the condensate particle size and can be expressed by the particle radius in the lognormal distribution power-law approximation:

$$f_{\text{sed}} = \frac{\int_0^\infty r^{3+\alpha} \frac{dn}{dr} dr}{r_w^\alpha \int_0^\infty r^3 \frac{dn}{dr} dr}, \quad (11)$$

which indicates that small f_{sed} encourages small cloud particle formation. The upward transport is stronger than the sedimentation when the cloud particles are small and vice-versa, which is in line with the experimental results in Figure B4 (a, b). The spectrum is sensitive to f_{sed} when this parameter has values between 10^{-1} and 10^{-3} , as shown in Fig. B4 (c), indicating the detectability of f_{sed} in this interval.

In our experiments, the particle radii are typically 1–10 μm , so they do not block the Rayleigh scattering slope caused by H_2 and H_2O at the optical wavelengths. For smaller radii (e.g., cyan line in Fig. B3), they are expected to contribute more to the optical spectrum, although theoretically it would be hard to form particles at very small sizes according to the nucleation theory in cloud formation ([Gao et al. 2018](#)). For any particle radii even smaller presented in this paper, it is just for model test purposes in extreme cases, and we make no efforts to show their detailed analysis here.

Radiative-inactive gases such as N_2 , if present, can change the atmospheric scale height. The increase of scale height decreases the transit depth and dampens its spectroscopic features, as illustrated in Fig. 3. As mentioned in previous sections, the presence of radiative-inactive gases cannot be detected directly through spectroscopic signatures. Opaque clouds may behave similarly to inactive gases in mitigating spectroscopic features, leading to potential degeneracy in retrieval experiments. Illustrated in Fig. 6, the comparison between Case 22 and 23 in Table 3 suggests the potential degeneracy between R_p , the baseline condensable gas abundance, T - p profile, and the N_2 abundance. In Case 23, we force $X_{\text{N}_2} = 0$ in the retrieval to monitor how *YunMa*

compensates for the missing gases in the atmosphere. Adjustment of R_p translates the transit depth without impact on spectroscopic features. The baseline condensable gas abundance and T - p profile are correlated to the formation of clouds. The results indicate that when N_2 is absent in prior, the mixing ratio of water vapour – the radiative-active gas – is significantly increased to compensate for the missing molecular weight, while more clouds are formed to further reduce the spectroscopic features. The decrease of T_{surf} helps in the same way. While the potential degeneracy exists from analysis and the results suggest the model behaviour in the case of missing radiative-inactive gases, the model chose from statistics the scenario closer to the ground truth in Case 22, showing the model’s potential in retrieving clouds in heavy atmospheres when it is not opaque.

As mentioned before, the cloud formation and T - p profile are correlated in *YunMa*. Therefore, the presence of optically thin clouds can help to constrain the T - p profile in retrievals: for instance, p_c , T_c and T_{surf} are well retrieved in Case 22. On the contrary, the T - p profile is not well constrained if clouds are completely absent (Case 25) or the microphysics part is removed from the retrieval (Case 24).

5.2. Cloud formation with the next-generation facilities’ data

With the high-quality transit spectra offered by the next-generation facilities, the uncertainties, wavelength coverage and spectral resolution will be significantly improved compared to most current data, and a simple opaque cloud model is insufficient for the transit study of next-generation data according to our results; the modelling of cloud radiative transfer and microphysics such as *YunMa* is needed. In our experiments, we chose a nominal 10 ppm as the observational uncertainty and found that clouds can be well-characterised in most experiments. With the next-generation data and *YunMa*, there are still limits in retrieving the featureless spectra. A smaller uncertainty may help in retrieving cloud parameters in the most difficult cases: we therefore adopted an unrealistic 1 ppm to test their detectability in an ideal case (Case 10, 15 and 7). With 1 ppm, the atmospheres were constrained well, although the spectra were featureless. Our experiments also suggest that broad wavelength coverage is paramount to characterising clouds well: here, optical wavelengths play a critical role when combined with infrared spectral coverage.

5.3. Numerical instabilities in cloud microphysics simulations

We have selected the explicit Runge-Kutta method of order 8 (DOP853, Hairer et al. 1988) to solve equa-

tion (2) as it delivered the most stable numerical performance for our experiments. However, numerical instabilities may occur when a large relative (*rtol*) and absolute (*atol*) tolerances are chosen. Sometimes the ODE solver cannot converge for q_t and indicates “no clouds” as a solution due to the numerical instability. Caution is also needed in estimating the cloud mixing ratio (q_c), as q_t might be two orders of magnitude larger than q_c and numerical errors could be injected when q_s is subtracted from q_t . When solving the ODE with too large tolerance, q_t might converge to a certain value, but q_c would be estimated as negligible according to equation (2 and 1). In other words, even though when the ODE solution for the gas phase seems numerically stable, it might not be precise and accurate enough. In those cases, the retrieval performances are affected, as shown in Fig. B5, where multiple islands of solutions in the posteriors are visible; these are caused by numerical instabilities, and the issue is more obvious for larger tolerance values. After many tests, we have decided to use “DOP853” in solving the ODE with $rtol = 1 \times 10^{-13}$ and $atol = 10^{-16}$, which guarantee numerically stable results.

6. CONCLUSIONS

YunMa is a state-of-art cloud model optimised for the interpretation of the next generation of exoplanetary atmospheric data, as provided by e.g., JWST, Roman, Twinkle and Ariel. These facilities will provide an unprecedented amount of high-quality data, where the cloud formation process and cloud scattering properties can no longer be ignored.

YunMa cloud microphysics is based on the model published by Ackerman & Marley (2001), while the scattering properties of clouds are calculated through the open-source B-H Mie code. When coupled to the *TauREx* framework (Al-Refaie et al. 2021), *YunMa* becomes a very versatile model which can simulate transit and eclipse spectra for a variety of cloudy exoplanets with different masses, atmospheric compositions and temperatures. Most importantly, *YunMa+TauREx* can be used as a spectral retrieval framework optimised for cloudy atmospheres. Here, the sedimentation efficiency, f_{sed} , is a critical parameter to control the cloud microphysics in the retrieval.

We have validated *YunMa* against previous work which also adopted the A-M approach. We have validated the radiative transfer calculations in *YunMa*, including cloud scattering, against PyMieScatt. Finally, we have validated *YunMa* against other cloud microphysics models published in the literature.

We have run over one hundred retrieval experiments with *YunMa*, with different cloud compositions (e.g., KCl, MgSiO₃, Fe clouds). In this paper, we have presented and discussed 28 cases of water clouds in the atmosphere of a temperate super-Earth, K2-18b-like. Through these experiments, we have learnt that *YunMa* is capable of retrieving accurately cloud formation parameters, as well as atmospheric trace gases' mixing ratios and thermal profiles when clouds are not so opaque to mask all the atmospheric features at most wavelengths. The optical wavelengths contain important scattering information of the cloud particles and are therefore critical for the correct extraction of the cloud formation parameters.

While the current version of *YunMa* can retrieve only one size of cloud particles at a time, the future version of *YunMa* will include the possibility of retrieving a distribution of the cloud particle sizes. 2-D cloud models, which include horizontal convection, will soon be within reach of computing speed and might be considered in future versions of *YunMa*.

The work presented in this paper was partially supported by UKSA, grant ST/X002616/1 and ST/W00254X/1, and ExoMolHD ERC grant 883830. QC is supported by the ESA Research Fellowship Program. The authors acknowledge the use of the UCL Kathleen High-Performance Computing Facility (Kathleen@UCL) and associated support services in completing this work. This work utilised the Cambridge Service for Data-Driven Discovery (CSD3), part of which is operated by the University of Cambridge Research Computing on behalf of the STFC DiRAC HPC Facility (www.dirac.ac.uk). The DiRAC component of CSD3 was funded by BEIS capital funding via STFC capital grants ST/P002307/1 and ST/R002452/1 and STFC operations grant ST/R00689X/1. DiRAC is part of the National e-Infrastructure.

We thank Dr Andrew S. Ackerman for the constructive communication on the A-M model and for sharing the original code, Dr Kai-Hou Yip and Sam Wright for suggestions on the numerical methods and Dr Yui Kawashima for the cloud and haze model discussion.

APPENDIX

A. SUPPLEMENTARY EQUATIONS

In Section 2.1.1, the SVP can be estimated with the Clausius-Clapeyron equation:

$$e_s = e_0 \exp \left[\frac{\ell}{R_{SV}} \left(\frac{1}{T_0} - \frac{1}{T} \right) \right], \quad (\text{A1})$$

where ℓ is the latent heat of evaporation, R_{SV} is the specific gas constant for the vapour, T is the atmospheric temperature, and T_0 is the temperature at vapour pressure e_0 . We use the results from laboratory measure-

ments of these parameters for the different chemical species when available.

β is the Cunningham slip factor:

$$\beta = 1 + 1.26N_{\text{Kn}}, \quad (\text{A2})$$

The Knudsen number (N_{Kn}) is the ratio between the molecular mean free path and the droplet radius.

YunMa adopts two ways to estimate η . One is that [Lavvas et al. \(2008\)](#) suggested to use:

$$\eta = \frac{1}{3}\rho_a\bar{V}\lambda_a, \quad (\text{A3})$$

where \bar{V} is the thermal velocity of gaseous components, and λ_a is the mean free path. Another uses the definition by [Rosner \(2012\)](#), which is also adopted by [Ackerman & Marley \(2001\)](#):

$$\eta = \frac{5}{16} \frac{\sqrt{\pi m k_B T}}{\pi d^2} \frac{(k_B T / \epsilon)^{0.16}}{1.22}, \quad (\text{A4})$$

where d is the diameter of a gas particle and ϵ is the atmospheric Lennard-Jones potential well depth. When using the A-M approach, v_f and the particle size are positively correlated using η either from [Rosner \(2012\)](#) or [Lavvas et al. \(2008\)](#).

In Section 2.1.2, assuming a lognormal cloud particle size distribution, the geometric mean (r_g) is defined as:

$$r_g = e \frac{\int_0^\infty \ln r \frac{dn}{dr} dr}{\int_0^\infty \frac{dn}{dr} dr}. \quad (\text{A5})$$

The power law approximation allows representation of f_{sed} using the particle size distribution.

$$f_{\text{sed}} \approx \frac{\int_0^\infty r^{3+\alpha} \frac{dn}{dr} dr}{r_w^\alpha \int_0^\infty r^3 \frac{dn}{dr} dr}, \quad (\text{A6})$$

where n is the accumulated number density as defined in Section 2 and σ_g is the geometric standard deviation of the lognormal particle radius distribution. Through an integration of the lognormal distribution, [Ackerman & Marley \(2001\)](#) derived that:

$$r_g = r_w f_{\text{sed}}^{\frac{1}{\alpha}} \exp\left(-\frac{\alpha+6}{2} \ln^2 \sigma_g\right), \quad (\text{A7})$$

where the σ_g is the geometric standard deviation of the particle radii.

The effective mean radius (r_{eff}) is the area-weighted average radius defined by [Hansen & Travis \(1974\)](#) to approximately represent the scattering properties of the whole size distribution by a single parameter when the particle radius is larger than the radiation wavelength.

To derive r_{eff} , we first recall that in lognormal distribution, the t -th raw moment is given by:

$$m_t = N_0 r_g \exp\left[\frac{(t\sigma)^2}{2}\right]. \quad (\text{A8})$$

Therefore r_{eff} , which is the area-weighted average radius, can be estimated through:

$$r_{\text{eff}} = \frac{\int_0^\infty r \pi r^2 \frac{dn}{dr} dr}{\int_0^\infty \pi r^2 \frac{dn}{dr} dr} = r_w f_{\text{sed}}^{\frac{1}{\alpha}} \exp\left(-\frac{\alpha+1}{2} \ln^2 \sigma_g\right). \quad (\text{A9})$$

Similarly, the total number density for the particles is estimated by using the volume-weighted mean:

$$N = \frac{3\varepsilon\rho_a q_c}{4\pi\rho_p r_g^3} \exp\left(-\frac{9}{2} \ln^2 \sigma_g\right). \quad (\text{A10})$$

B. SUPPLEMENTARY FIGURES

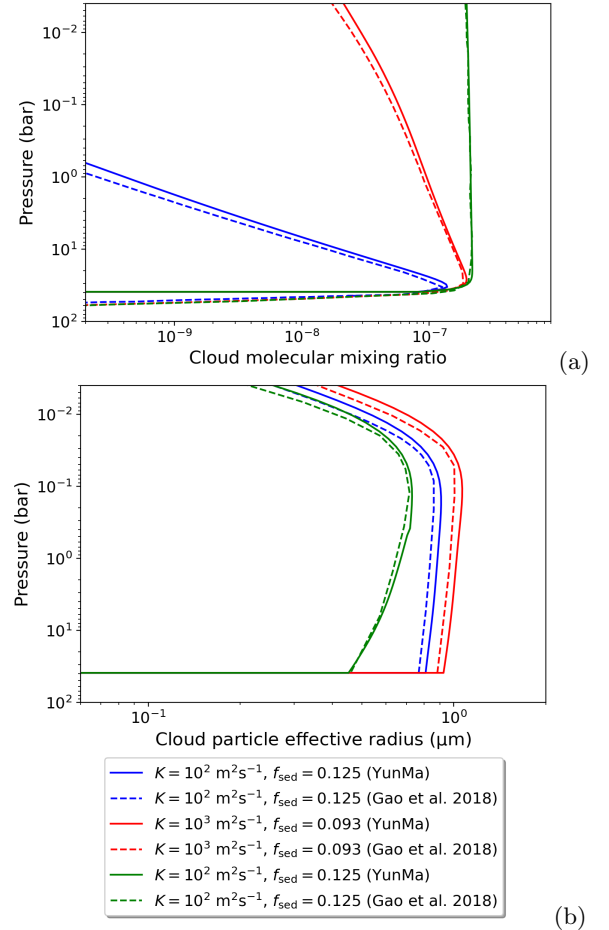


Figure B1. Validation of *YunMa* (solid lines) against the A-M model in [Gao et al. \(2018\)](#) (dashed lines). Top: condensate mixing ratios. Bottom: cloud particle effective mean radii.

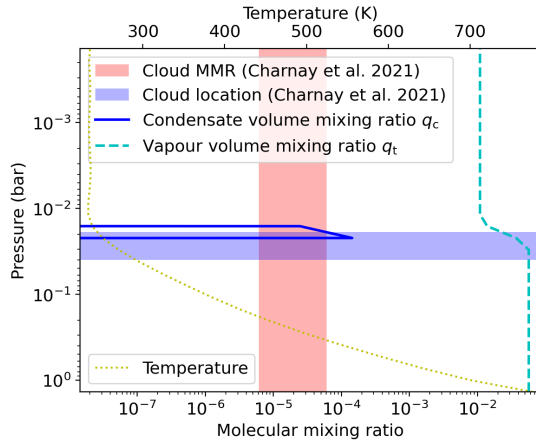


Figure B2. Comparison of *YunMa*'s results against simulations by Charnay et al. (2021 b) for the $100 \times$ solar metallicity scenario (see Fig. 6 (a) of the substellar region). The results are consistent, despite being generated by a 1-D cloud microphysical model in this work and the MIT General Circulation Model (Campin et al. 2022) in the case of Charnay et al. (2021 b).

REFERENCES

- Ackerman, A. S., & Marley, M. S. 2001, *The Astrophysical Journal*, 556, 872
- Adams, D. J., Kataria, T., Batalha, N. E., Gao, P., & Knutson, H. A. 2022, *ApJ*, 926, 157, doi: [10.3847/1538-4357/ac3d32](https://doi.org/10.3847/1538-4357/ac3d32)
- Al-Refaie, A. F., Changeat, Q., Venot, O., Waldmann, I. P., & Tinetti, G. 2022, *The Astrophysical Journal*, 932, 123, doi: [10.3847/1538-4357/ac6dcd](https://doi.org/10.3847/1538-4357/ac6dcd)
- Al-Refaie, A. F., Changeat, Q., Waldmann, I. P., & Tinetti, G. 2019, arXiv preprint arXiv:1912.07759
- Al-Refaie, A. F., Changeat, Q., Waldmann, I. P., & Tinetti, G. 2021, *The Astrophysical Journal*, 917, 37, doi: [10.3847/1538-4357/ac0252](https://doi.org/10.3847/1538-4357/ac0252)
- Barstow, J. K. 2020, *MNRAS*, 497, 4183, doi: [10.1093/mnras/staa2219](https://doi.org/10.1093/mnras/staa2219)
- Batalha, N. E., Marley, M. S., Lewis, N. K., & Fortney, J. J. 2019, *ApJ*, 878, 70, doi: [10.3847/1538-4357/ab1b51](https://doi.org/10.3847/1538-4357/ab1b51)
- Baudino, J. L., Bézard, B., Boccaletti, A., et al. 2015, *A&A*, 582, A83, doi: [10.1051/0004-6361/201526332](https://doi.org/10.1051/0004-6361/201526332)
- Bean, J. L., Stevenson, K. B., Batalha, N. M., et al. 2018, *PASP*, 130, 114402, doi: [10.1088/1538-3873/aadbf3](https://doi.org/10.1088/1538-3873/aadbf3)
- Benneke, B. 2015, arXiv e-prints, arXiv:1504.07655. <https://arxiv.org/abs/1504.07655>
- Benneke, B., Knutson, H. A., Lothringer, J., et al. 2019 a, *Nature Astronomy*, 3, 813
- Bohren, C. F., & Huffman, D. R. 2008, *Absorption and scattering of light by small particles* (John Wiley & Sons)
- Boucher, A., Darveau-Bernier, A., Pelletier, S., et al. 2021, *AJ*, 162, 233, doi: [10.3847/1538-3881/ac1f8e](https://doi.org/10.3847/1538-3881/ac1f8e)
- Broggi, M., & Line, M. R. 2019, *AJ*, 157, 114, doi: [10.3847/1538-3881/aafdd3](https://doi.org/10.3847/1538-3881/aafdd3)
- Burrows, A. S. 2014, *Nature*, 513, 345, doi: [10.1038/nature13782](https://doi.org/10.1038/nature13782)
- Caldas, A., Leconte, J., Selsis, F., et al. 2019, *A&A*, 623, A161, doi: [10.1051/0004-6361/201834384](https://doi.org/10.1051/0004-6361/201834384)
- Campin, J.-M., Heimbach, P., Losch, M., et al. 2022, MITgcm/MITgcm: checkpoint68i, checkpoint68i, Zenodo, doi: [10.5281/zenodo.6498956](https://doi.org/10.5281/zenodo.6498956)
- Carlson, B. E., Rossow, W. B., & Orton, G. S. 1988, *Journal of Atmospheric Sciences*, 45, 2066
- Changeat, Q., Al-Refaie, A. F., Edwards, B., Waldmann, I. P., & Tinetti, G. 2021a, *ApJ*, 913, 73, doi: [10.3847/1538-4357/abf2bb](https://doi.org/10.3847/1538-4357/abf2bb)
- Changeat, Q., Edwards, B., Al-Refaie, A. F., et al. 2021b, *Experimental Astronomy*, doi: [10.1007/s10686-021-09794-w](https://doi.org/10.1007/s10686-021-09794-w)
- Changeat, Q., Edwards, B., Al-Refaie, A. F., et al. 2022, *ApJS*, 260, 3, doi: [10.3847/1538-4365/ac5cc2](https://doi.org/10.3847/1538-4365/ac5cc2)
- Charnay, B., Bézard, B., Baudino, J. L., et al. 2018, *ApJ*, 854, 172, doi: [10.3847/1538-4357/aaac7d](https://doi.org/10.3847/1538-4357/aaac7d)
- Charnay, B., Blain, D., Bézard, B., et al. 2021 b, *Astronomy & Astrophysics*, 646, A171
- Charnay, B., Tobie, G., Lebonnois, S., & Lorenz, R. D. 2022, *A&A*, 658, A108, doi: [10.1051/0004-6361/202141898](https://doi.org/10.1051/0004-6361/202141898)

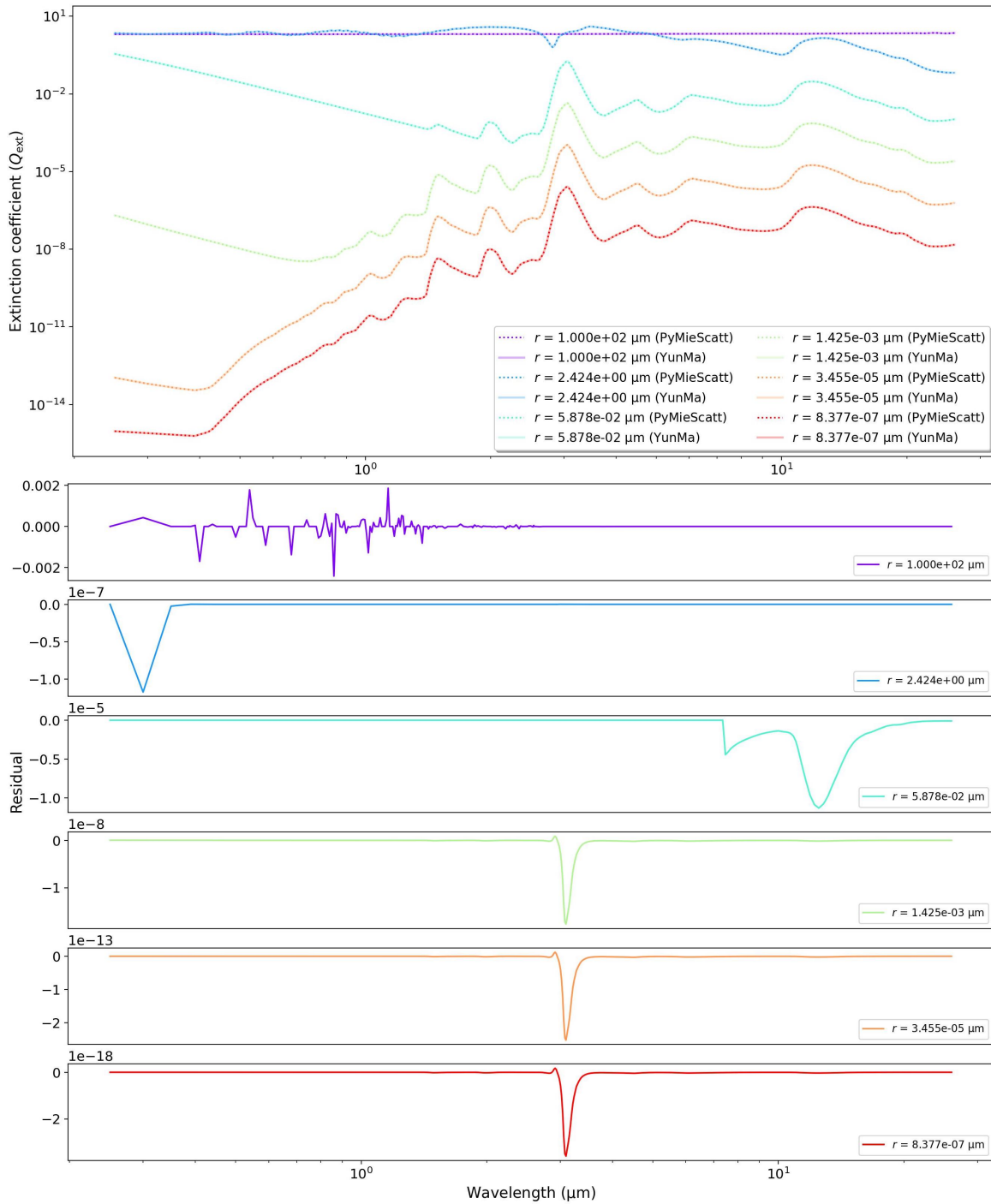


Figure B3. Validation of radiative transfer simulations obtained with *YunMa* against the open source code PyMieScatt (Sumlin et al. 2018). The extinction coefficients for cloud particles with different sizes are estimated from the theory of Bohren & Huffman (2008). To address the computational limitations of retrievals, we pre-calculated the extinction coefficients used in equation (8) to estimate the cross-sections of the cloud particles. The pre-calculated list includes values for particle radii from 1×10^{-7} to 1×10^{-2} μm , equally spaced in the logarithm space. Here we show only six examples in the top panel. Bottom panels: residuals obtained by subtracting the extinction coefficients as estimated by the two codes, *YunMa* and PyMieScatt. The maximum discrepancy, corresponding to the largest particle radius simulated here ($r = 1 \times 10^2$), is negligible, i.e. ± 0.002 .

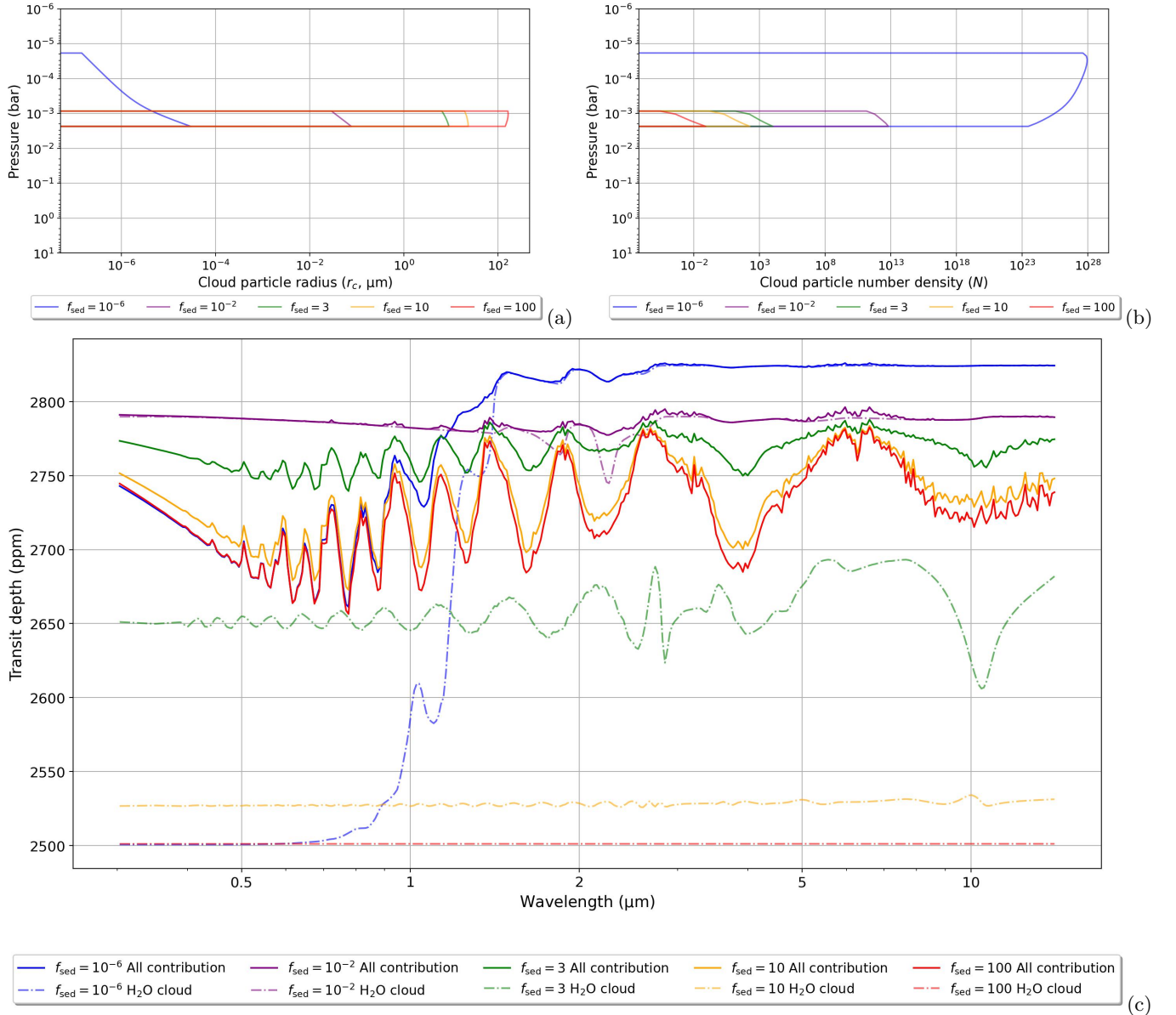


Figure B4. Test results for r_{eff} (top left), N (top right) and the transit spectrum (bottom) with different sedimentation efficiency f_{sed} . The cloud layer shrinks with the increasing of f_{sed} .

Cox, A. N. 2015, *Allen's Astrophysical Quantities* (Springer)

Cubillos, P. E., & Bleic, J. 2021, *MNRAS*, 505, 2675, doi: [10.1093/mnras/stab1405](https://doi.org/10.1093/mnras/stab1405)

Drummond, B., Tremblin, P., Baraffe, I., et al. 2016, *A&A*, 594, A69, doi: [10.1051/0004-6361/201628799](https://doi.org/10.1051/0004-6361/201628799)

Edwards, B., Rice, M., Zingales, T., et al. 2019, *Experimental Astronomy*, 47, 29

Edwards, B., Changeat, Q., Tsiaras, A., et al. 2022, arXiv e-prints, arXiv:2211.00649.

<https://arxiv.org/abs/2211.00649>

Fleck, J. A., J., & Canfield, E. H. 1984, *Journal of Computational Physics*, 54, 508,

doi: [10.1016/0021-9991\(84\)90130-X](https://doi.org/10.1016/0021-9991(84)90130-X)

Fortney, J. J., Barstow, J. K., & Madhusudhan, N. 2021, in *ExoFrontiers; Big Questions in Exoplanetary Science*, ed. N. Madhusudhan, 17–1,

doi: [10.1088/2514-3433/abfa8fch17](https://doi.org/10.1088/2514-3433/abfa8fch17)

Gandhi, S., & Madhusudhan, N. 2018, *MNRAS*, 474, 271, doi: [10.1093/mnras/stx2748](https://doi.org/10.1093/mnras/stx2748)

Gao, P., Marley, M. S., & Ackerman, A. S. 2018, *The Astrophysical Journal*, 855, 86

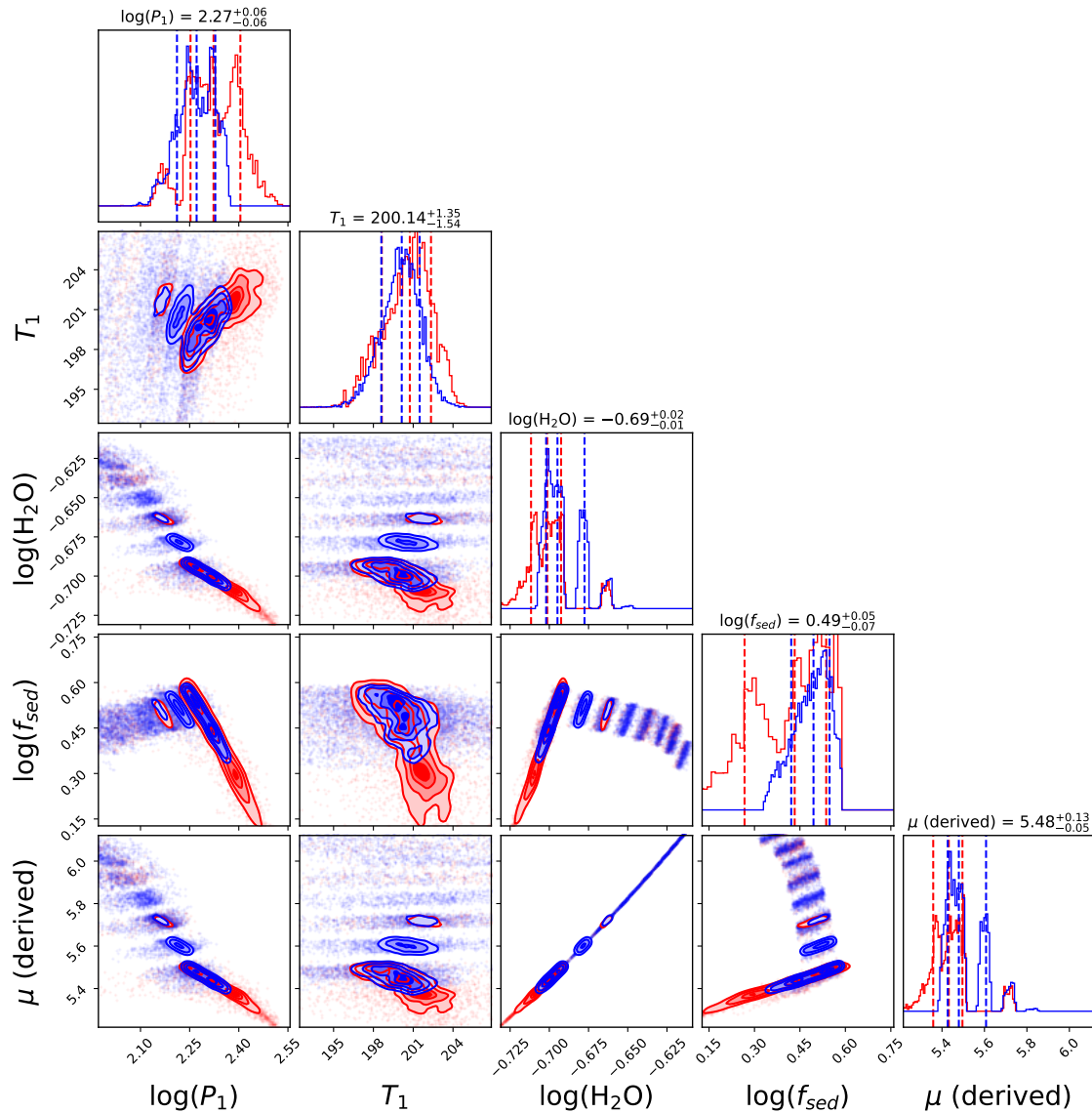


Figure B5. Example of numerical instability in cloud formation simulations when large relative ($rtol$) and absolute ($atol$) tolerances are chosen in solving equation (2) with Runge-Kutta method. Blue plots: $rtol = 1 \times 10^{-8}$ and $atol = 1 \times 10^{-12}$. Red plots: $rtol = 1 \times 10^{-12}$ and $atol = 1 \times 10^{-15}$. In these tests, the retrieval performances are affected by numerical instability, as illustrated in this figure where multiple islands of solutions in the posteriors are clearly visible.

Gao, P., Thorngren, D. P., Lee, E. K. H., et al. 2020, Nature Astronomy, 4, 951, doi: [10.1038/s41550-020-1114-3](https://doi.org/10.1038/s41550-020-1114-3)

Gardner, J. P., Mather, J. C., Clampin, M., et al. 2006, Space Science Reviews, 123, 485

Gierasch, P., & Conrath, B. 1985, Recent Advances in Planetary Meteorology, 121

Goyal, J. M., Mayne, N., Sing, D. K., et al. 2017, Monthly Notices of the Royal Astronomical Society, 474, 5158, doi: [10.1093/mnras/stx3015](https://doi.org/10.1093/mnras/stx3015)

Greene, T. P., Line, M. R., Montero, C., et al. 2016, ApJ, 817, 17, doi: [10.3847/0004-637X/817/1/17](https://doi.org/10.3847/0004-637X/817/1/17)

Hairer, E., Norsett, S. P., & Wanner, G. 1988, Solving Ordinary Differential Equations. I: Nonstiff Problems (Springer Science & Business Media)

Hansen, J. E., & Travis, L. D. 1974, SSRv, 16, 527, doi: [10.1007/BF00168069](https://doi.org/10.1007/BF00168069)

Harrington, J., Himes, M. D., Cubillos, P. E., et al. 2022, PSJ, 3, 80, doi: [10.3847/PSJ/ac3513](https://doi.org/10.3847/PSJ/ac3513)

Helling, C. 2022, arXiv e-prints, arXiv:2205.00454. <https://arxiv.org/abs/2205.00454>

Helling, C., Iro, N., Corrales, L., et al. 2019, A&A, 631, A79, doi: [10.1051/0004-6361/201935771](https://doi.org/10.1051/0004-6361/201935771)

- Helling, C., Samra, D., Lewis, D., et al. 2022, arXiv e-prints, arXiv:2208.05562.
<https://arxiv.org/abs/2208.05562>
- Husser, T. O., Wende-von Berg, S., Dreizler, S., et al. 2013, *A&A*, 553, A6, doi: [10.1051/0004-6361/201219058](https://doi.org/10.1051/0004-6361/201219058)
- Irwin, P., Teanby, N., De Kok, R., et al. 2008, *Journal of Quantitative Spectroscopy and Radiative Transfer*, 109, 1136
- JWST Transiting Exoplanet Community Early Release Science Team. 2022, *Nature*, doi: [10.1038/s41586-022-05269-w](https://doi.org/10.1038/s41586-022-05269-w)
- Karman, T., Gordon, I. E., van der Avoird, A., et al. 2019, *Icarus*, 328, 160, doi: [10.1016/j.icarus.2019.02.034](https://doi.org/10.1016/j.icarus.2019.02.034)
- Kawashima, Y., & Ikoma, M. 2018, *The Astrophysical Journal*, 853, 7
- Kitzmann, D., Heng, K., Oreshenko, M., et al. 2020, *ApJ*, 890, 174, doi: [10.3847/1538-4357/ab6d71](https://doi.org/10.3847/1538-4357/ab6d71)
- Kreidberg, L., Bean, J. L., Désert, J.-M., et al. 2014, *Nature*, 505, 69
- Lavvas, P., Coustenis, A., & Vardavas, I. 2008, *Planetary and Space Science*, 56, 67
- Lee, J. M., Fletcher, L. N., & Irwin, P. G. J. 2012, *MNRAS*, 420, 170, doi: [10.1111/j.1365-2966.2011.20013.x](https://doi.org/10.1111/j.1365-2966.2011.20013.x)
- Lewis, J. S. 1969, *Icarus*, 10, 365
- Line, M. R., Wolf, A. S., Zhang, X., et al. 2013, *The Astrophysical Journal*, 775, 137
- Lueber, A., Kitzmann, D., Bowler, B. P., Burgasser, A. J., & Heng, K. 2022, *ApJ*, 930, 136, doi: [10.3847/1538-4357/ac63b9](https://doi.org/10.3847/1538-4357/ac63b9)
- Lunine, J. I., Hubbard, W., Burrows, A., Wang, Y.-P., & Garlow, K. 1989, *The Astrophysical Journal*, 338, 314
- MacDonald, R. J., & Madhusudhan, N. 2017, *Monthly Notices of the Royal Astronomical Society*, 469, 1979
- Madhusudhan, N. 2019, *Annual Review of Astronomy and Astrophysics*, 57, 617
- Madhusudhan, N., Nixon, M. C., Welbanks, L., Piette, A. A., & Booth, R. A. 2020, *The Astrophysical Journal Letters*, 891, L7
- Madhusudhan, N., & Seager, S. 2009, *ApJ*, 707, 24, doi: [10.1088/0004-637X/707/1/24](https://doi.org/10.1088/0004-637X/707/1/24)
- Mai, C., & Line, M. R. 2019, *ApJ*, 883, 144, doi: [10.3847/1538-4357/ab3e6d](https://doi.org/10.3847/1538-4357/ab3e6d)
- Marley, M. S., Gelino, C., Stephens, D., Lunine, J. I., & Freedman, R. 1999, *The Astrophysical Journal*, 513, 879
- Min, M., Ormel, C. W., Chubb, K., Helling, C., & Kawashima, Y. 2020, *Astronomy & Astrophysics*, 642, A28
- Min, M., Hovenier, J. W., & de Koter, A. 2005, *A&A*, 432, 909, doi: [10.1051/0004-6361:20041920](https://doi.org/10.1051/0004-6361:20041920)
- Mollière, P., Wardenier, J. P., van Boekel, R., et al. 2019, *A&A*, 627, A67, doi: [10.1051/0004-6361/201935470](https://doi.org/10.1051/0004-6361/201935470)
- Mollière, P., Stolker, T., Lacour, S., et al. 2020, *A&A*, 640, A131, doi: [10.1051/0004-6361/202038325](https://doi.org/10.1051/0004-6361/202038325)
- Nixon, M. C., & Madhusudhan, N. 2022, *ApJ*, 935, 73, doi: [10.3847/1538-4357/ac7c09](https://doi.org/10.3847/1538-4357/ac7c09)
- Ormel, C. W., & Min, M. 2019, *A&A*, 622, A121, doi: [10.1051/0004-6361/201833678](https://doi.org/10.1051/0004-6361/201833678)
- Pinhas, A., Madhusudhan, N., Gandhi, S., & MacDonald, R. 2019, *MNRAS*, 482, 1485, doi: [10.1093/mnras/sty2544](https://doi.org/10.1093/mnras/sty2544)
- Polyansky, O. L., Kyuberis, A. A., Zobov, N. F., et al. 2018, *Monthly Notices of the Royal Astronomical Society*, 480, 2597, doi: [10.1093/mnras/sty1877](https://doi.org/10.1093/mnras/sty1877)
- Robbins-Blanch, N., Kataria, T., Batalha, N. E., & Adams, D. J. 2022, *ApJ*, 930, 93, doi: [10.3847/1538-4357/ac658c](https://doi.org/10.3847/1538-4357/ac658c)
- Rooney, C. M., Batalha, N. E., Gao, P., & Marley, M. S. 2022, *ApJ*, 925, 33, doi: [10.3847/1538-4357/ac307a](https://doi.org/10.3847/1538-4357/ac307a)
- Rosner, D. E. 2012, *Transport processes in chemically reacting flow systems (Courier Corporation)*
- Roudier, G. M., Swain, M. R., Gudipati, M. S., et al. 2021, *AJ*, 162, 37, doi: [10.3847/1538-3881/abfdad](https://doi.org/10.3847/1538-3881/abfdad)
- Sing, D. K., Fortney, J. J., Nikolov, N., et al. 2016, *Nature*, 529, 59
- Stevenson, K. B. 2016, *The Astrophysical Journal*, 817, L16, doi: [10.3847/2041-8205/817/2/L16](https://doi.org/10.3847/2041-8205/817/2/L16)
- Sumlin, B. J., Heinson, W. R., & Chakrabarty, R. K. 2018, *JQSRT*, 205, 127, doi: [10.1016/j.jqsrt.2017.10.012](https://doi.org/10.1016/j.jqsrt.2017.10.012)
- Tennyson, J., & Yurchenko, S. N. 2012, *Monthly Notices of the Royal Astronomical Society*, 425, 21
- Tennyson, J., & Yurchenko, S. N. 2021, *Astronomy and Geophysics*, 62, 6.16, doi: [10.1093/astrog/atab102](https://doi.org/10.1093/astrog/atab102)
- Tinetti, G., Encrenaz, T., & Coustenis, A. 2013, *A&A Rv*, 21, 63, doi: [10.1007/s00159-013-0063-6](https://doi.org/10.1007/s00159-013-0063-6)
- Tinetti, G., Drossart, P., Eccleston, P., et al. 2018, *Experimental Astronomy*, 46, 135
- Tinetti, G., Eccleston, P., Haswell, C., et al. 2021, arXiv e-prints, arXiv:2104.04824.
<https://arxiv.org/abs/2104.04824>
- Toon, O. B., Turco, R. P., Hamill, P., Kiang, C. S., & Whitten, R. C. 1979, *Journal of Atmospheric Sciences*, 36, 718, doi: [10.1175/1520-0469\(1979\)036<0718:AODMDA>2.0.CO;2](https://doi.org/10.1175/1520-0469(1979)036<0718:AODMDA>2.0.CO;2)
- Tremblin, P., Amundsen, D. S., Mourier, P., et al. 2015, *The Astrophysical Journal*, 804, L17, doi: [10.1088/2041-8205/804/1/L17](https://doi.org/10.1088/2041-8205/804/1/L17)
- Tsai, S.-M., Innes, H., Lichtenberg, T., et al. 2021, *ApJL*, 922, L27, doi: [10.3847/2041-8213/ac399a](https://doi.org/10.3847/2041-8213/ac399a)
- Tsiaras, A., Waldmann, I. P., Tinetti, G., Tennyson, J., & Yurchenko, S. N. 2019, *Nature Astronomy*, 3, 1086

- Tsiaras, A., Waldmann, I. P., Zingales, T., et al. 2018, *AJ*, 155, 156, doi: [10.3847/1538-3881/aaaf75](https://doi.org/10.3847/1538-3881/aaaf75)
- Turco, R. P., Hamill, P., Toon, O. B., Whitten, R. C., & Kiang, C. S. 1979, *Journal of Atmospheric Sciences*, 36, 699, doi: [10.1175/1520-0469\(1979\)036<0699:AODMDA>2.0.CO;2](https://doi.org/10.1175/1520-0469(1979)036<0699:AODMDA>2.0.CO;2)
- Venot, O., Parmentier, V., Blecic, J., et al. 2020, *The Astrophysical Journal*, 890, 176
- Wakeford, H. R., Sing, D. K., Deming, D., et al. 2018, *AJ*, 155, 29, doi: [10.3847/1538-3881/aa9e4e](https://doi.org/10.3847/1538-3881/aa9e4e)
- Wang, F., Fujii, Y., & He, J. 2022, *The Astrophysical Journal*, 931, 48, doi: [10.3847/1538-4357/ac67e5](https://doi.org/10.3847/1538-4357/ac67e5)
- Warren, S. G., & Brandt, R. E. 2008, *Journal of Geophysical Research (Atmospheres)*, 113, D14220, doi: [10.1029/2007JD009744](https://doi.org/10.1029/2007JD009744)
- Welbanks, L., & Madhusudhan, N. 2021, *ApJ*, 913, 114, doi: [10.3847/1538-4357/abee94](https://doi.org/10.3847/1538-4357/abee94)
- Welbanks, L., Madhusudhan, N., Allard, N. F., et al. 2019, *ApJL*, 887, L20, doi: [10.3847/2041-8213/ab5a89](https://doi.org/10.3847/2041-8213/ab5a89)
- Windsor, J. D., Robinson, T. D., Koppurapu, R. k., et al. 2022, arXiv e-prints, arXiv:2210.10004. <https://arxiv.org/abs/2210.10004>
- Xuan, J. W., Wang, J., Ruffio, J.-B., et al. 2022, *ApJ*, 937, 54, doi: [10.3847/1538-4357/ac8673](https://doi.org/10.3847/1538-4357/ac8673)
- Yu, X., Moses, J. I., Fortney, J. J., & Zhang, X. 2021, *The Astrophysical Journal*, 914, 38, doi: [10.3847/1538-4357/abfdc7](https://doi.org/10.3847/1538-4357/abfdc7)
- Zhang, M., Chachan, Y., Kempton, E. M. R., Knutson, H. A., & Chang, W. H. 2020, *ApJ*, 899, 27, doi: [10.3847/1538-4357/abae6](https://doi.org/10.3847/1538-4357/abae6)